Spectroscopic and Theoretical Description of the Electronic Structure of $S = 3/2$ Iron−Nitrosyl Complexes and Their Relation to O_2 Activation by Non-Heme Iron Enzyme Active Sites

Carl A. Brown,† Mark A. Pavlosky,† Tami E. Westre,† Yan Zhang,† Britt Hedman,‡ Keith O. Hodgson,‡ and Edward I. Solomon*,†

Contribution from the Department of Chemistry and Stanford Synchrotron Radiation Laboratory, Stanford University, Stanford, California 94305

Received August 17, 1994[⊗]

Abstract: NO forms reversible complexes with non-heme ferrous enzymes and model complexes which exhibit unusual $S = 3/2$ ground states. These nitrosyl derivatives can serve as stable analogs of possible oxygen intermediates in the non-heme iron enzymes. Two complexes, $Fe(Me_3TACN)(NO)(N_3)_2$ and FeEDTA−NO, have been studied in detail using X-ray absorption, resonance Raman, absorption, magnetic circular dichroism, and electron paramagnetic resonance spectroscopies and SQUID magnetic susceptibility. These studies have been complemented by spin restricted and spin unrestricted SCF-Xα-SW electronic structure calculations. The description generated involves high spin Fe^{3+} antiferromagnetically coupled to NO^- $S = 1$. This description is strongly supported by experiment (X-ray absorption pre-edge multiplets and edge energy and shape, extended X-ray absorption fine structure bond lengths, resonance Raman force constants, ligand field and charge transfer spectral assignments), which also show that starting from the Fe^{3+}−NO^- limit the NO^- is involved in a strong donor bonding interaction to the Fe^{3+}. This donor bonding interaction involves the $4\sigma^+$ molecular orbital of the NO^- which is σ antibonding with respect to the NO bond and greatly strengthens this bond. The Fe−NO bond is bent in both complexes with an angle of 156° which the resonance Raman studies and SCF-Xα-SW calculations show derives from the stabilizing effect of bending on the in-plane bonding interaction of the NO^- π^* orbital with the d orbital on the iron. Magnetic circular dichroism data allow this study to be correlated with the nitrosyl derivative of the non-heme iron site in soybean lipoxygenase and demonstrate an analogous electronic structure description. As these calculations have been strongly supported by experiment for the nitrosyl complexes, they have been extended to possible oxygen intermediates. In parallel with the Fe^{3+}−NO^- complexes, the description of the intermediate obtained involves superoxide antiferromagnetically coupled to a high spin ferric center with a strong σ donation of charge from the superoxide to the iron. These studies allow spectral data on the nitrosyl complexes to be used to estimate bonding differences in possible oxygen intermediates of different non-heme iron proteins and provide insight into the activation of superoxide by coordination to the ferric center for reaction or further reduction.

Introduction

Mononuclear non-heme iron centers are present in the catalytic cycle of a number of proteins involved in oxygen activation.[1,2] In order to understand the reactivity of these systems, it is necessary to have a detailed description of the electronic as well as geometric structure of the non-heme iron active site.[3] Mononuclear ferrous active sites are generally considered difficult to probe experimentally since they are often electron paramagnetic resonance (EPR) inactive and do not exhibit low energy ligand to metal charge transfer transitions. Recently, a protocol has been developed to probe these sites in detail using a combination of absorption, circular dichroism (CD), and variable-temperature, variable-field magnetic circular dichroism (MCD) spectroscopies.[3] Since most of these systems are involved in oxygen activation, identification of oxygen intermediates during the catalytic cycle is necessary to obtain insight into reactivity at the molecular level. These intermediates, however, are often very short-lived and difficult to study experimentally.

As a probe of non-heme iron active sites, nitric oxide has been shown to react with the ferrous state of many mononuclear non-heme iron enzymes, *e.g.*, soybean lipoxygenase,[4,5] protocatechuate 4,5-dioxygenase,[6] metapyrocatechase,[7] putidamonooxin,[8] and isopenicillin N synthase,[9] to form stable nitrosyl complexes which can serve as reversible analogs of the possible dioxygen intermediates involved in catalysis. In the NO derivative of soybean lipoxygenase (SBL), as in most non-heme iron enzyme nitrosyl derivatives, an $S = 3/2$ ground state is generated.[5] This species is EPR active, and its distinctive $S = 3/2$ EPR signal allows one to probe non-heme ferrous complexes which are normally EPR silent. For intra- and extradiol dioxygenases Fe−NO EPR has been used as an analytical probe of substrate and water coordination through superhyperfine

* To whom correspondence should be addressed.
† Department of Chemistry.
‡ Stanford Synchrotron Radiation Laboratory.
⊗ Abstract published in *Advance ACS Abstracts*, December 15, 1994.
(1) Feig, A. L.; Lippard, S. J. *Chem. Rev.* **1994**, *94*, 759.
(2) Howard, J. B.; Rees, D. C. *Advances in Protein Chemistry*; Academic Press: New York, 1991; Vol. 42, p 199.
(3) Solomon, E. I.; Zhang, Y. *Acc. Chem. Res.* **1992**, *25*, 343.
(4) Nelson, M. J. *J. Biol. Chem.* **1987**, *262*, 12137.
(5) Galpin, J. R.; Veldink, G. A.; Vliegenthart, J. F. G.; Goldingh, J. *Biochim. Biophys. Acta* **1978**, *536*, 356.
(6) Arciero, D. M.; Lipscomb, J. D. *J. Biol. Chem.* **1986**, *261*, 2170.
(7) Arciero, D. M.; Orville, A. M.; Lipscomb, J. D. *J. Biol. Chem.* **1985**, *260*, 14035.
(8) Twilfer, H.; Bernhardt, F.-H.; Gersonde, K. *Eur. J. Biochem.* **1985**, *147*, 171.
(9) Chen, V. J.; Orville, A. M.; Harpel, M. R.; Frolik, C. A.; Surerus, K. K.; Münck, E.; Lipscomb, J. D. *J. Biol. Chem.* **1989**, *264*, 21677.

0002-7863/95/1517-0715$09.00/0

effects on the spectrum.[6,7] Mössbauer spectroscopy has also proved to be a very useful analytical probe,[10,11] but conflicting descriptions of the electronic origin of the $S = 3/2$ ground state have been suggested. The Mössbauer isomer shift for the NO complex of protocatechuate 4,5-dioxygenase has been used to argue against a ferric configuration,[12] while the equivalent isomer shift for the substrate−NO ternary complex of putidamonooxin has been used to support its description as an intermediate spin ferric site.[8]

The description of metal−nitrosyl complexes is a problem of both theoretical and experimental interest. An early classic review by Enemark and Feltham gives a basic description of metal−nitrosyl complexes and their bonding.[13] In the Enemark/Feltham notation, the metal−nitrosyl unit is described as a discrete unit, *i.e.*, $\{MNO\}^n$, where n represents the sum of the metal d and NO π^* electrons.[13] The Fe−NO species generated in non-heme ferrous enzymes is thus designated $\{FeNO\}^7$. A variety of descriptions of the electronic structure of these complexes have been put forth in the literature. These include [Fe^+ d^7 ($S = 3/2$)−NO^+ ($S = 0$)],[14] [Fe^{2+} d^6 ($S = 2$)−NO^0 ($S = 1/2$)] antiferromagnetically coupled,[15] [Fe^{3+} d^5 ($S = 1/2$)−NO^- ($S = 1$)] ferromagnetically coupled,[16] and [Fe^{3+} d^5 ($S = 3/2$)−NO^- ($S = 0$)].[11] None of these descriptions, however, are consistent with all of the experimental and theoretical data that exist.

Recently, a new description, [Fe^{3+} d^5 ($S = 5/2$)−NO^- ($S = 1$)] antiferromagnetically coupled, was communicated.[17] A combination of absorption, variable-temperature, variable-field MCD, resonance Raman, EPR, and X-ray absorption (XAS) spectroscopies, magnetism, and theoretical calculations (SCF-Xα-SW) was used to initially characterize two inorganic $S = 3/2$ model complexes and the active site of SBL−NO.[17] These studies indicated that the iron is best described as high spin ferric ($S = 5/2$) and the NO as NO^- ($S = 1$) which are spin coupled antiferromagnetically to produce the correct total spin state of $S = 3/2$. Since the description of the iron as purely ferric or ferrous is simplistic, a more quantitative description of the electronic structure is necessary to understand its relevance to the reactivity of ferrous sites with dioxygen. The purpose of this study is to follow up on our earlier communication with a more complete description of the distinctive $\{FeNO\}^7$, $S = 3/2$ unit and its relevance as a model of oxygen bonding in the bioinorganic chemistry of non-heme iron proteins.

The inorganic complexes studied are $Fe[Me_3TACN](NO)(N_3)_2$, where Me_3TACN is *N,N′,N″*-trimethyl-1,4,7-triazacyclononane, hereafter designated by **1**, and FeEDTA−NO, where EDTA is ethylenediaminetetraacetic acid, designated by **2**. Both of these complexes form a $\{FeNO\}^7$ unit with an $S = 3/2$ ground state.[18] Complex **1** has been structurally characterized and has an FeNO angle of 155.5°. Until the studies presented here, no detailed spectroscopic information had been obtained on **1**. Complex **2**, on the other hand, has been studied through Mössbauer and EPR to elucidate its ground state properties.[19,12,20] The study of complex **2** has been limited by the fact that this complex has not been crystallographically characterized and thus the FeNO angle is not known. The question of the FeNO angle and bond lengths of **2** has been resolved recently using an extended X-ray absorption fine structure (EXAFS) multiple scattering analysis by GNXAS (a new theoretical EXAFS data analysis package).[21,22] Multiple scattering effects have previously been used in certain special circumstances to extract angle information in inorganic complexes using empirical data analysis.[23,24] However, the use of theoretical parameters coupled with a general treatment of three-body correlated motion and Debye−Waller factors in GNXAS provides for a general approach to angle determination which does not rely on models. GNXAS was therefore used to analyze a number of crystallographically characterized $\{FeNO\}^7$ complexes and then applied to **2**, for which an FeNO angle of 156° was found.[21] This angle is identical within error to that observed for complex **1**, indicating that the electronic and geometric structures of this unit are coupled.

A detailed description of the electronic structure of the $\{FeNO\}^7$ unit is developed below. A combination of experimental (X-ray absorption, EPR, SQUID magnetic susceptibility, resonance Raman spectroscopy, near-IR/visible/UV absorption, and MCD) and theoretical (SCF-Xα-SW calculations) methods has been used. The results of each technique and the calculations will be analyzed in turn. Assignments of the absorption spectrum will be made which are consistent with all of the techniques employed. This experimental and theoretical description of the NO interaction with non-heme iron is then extended to model the dioxygen interaction with a non-heme Fe center using SCF-Xα-SW calculations. Finally in the Discussion, the electronic structure of the FeNO unit and its relation to spectral features are summarized. The relation of these spectral features to differences in FeNO bonding is described, and the FeNO bonding description is extended to $\{FeO_2\}^8$ bonding and its relation to protein reactivity.

Experimental Section

Complex **2** was prepared by the following procedure. All chemicals, apparatus, and solvents were thoroughly purged with nitrogen or argon prior to use. Ferrous EDTA ($[Fe(OH_2)EDTA]^{2-}$) solution, 50 mM in Fe, was prepared by anaerobic addition of ferrous ammonium sulfate to a 60 mM solution of Na_2EDTA in pH 6.5, 0.1 M deoxygenated phosphate buffer. Nitric oxide (Matheson Inc.) was bubbled through the solution for approximately 20 min, or until the solution stopped changing color, indicating completion of the reaction. The sample of **2** for SQUID measurements was prepared in D_2O and deuterated phosphate buffer. Complex **1** was prepared according to the published procedure.[16] Note that there was an error on the relative amount of each reactant used in the original paper. The $Fe:L:N_3^-$ ratio actually used in this synthesis was 1:1:2 (not 0.42:1:1).[16] For X-ray absorption studies on the EDTA series the $[Fe(OH_2)EDTA]^{2-}$ solution was prepared as above; oxidizing this solution produced $[Fe(OH_2)EDTA]^-$. $[Fe(TMC)NO](BF_4)_2$,[25] $[Fe(TMC)N_3](BF_4)$,[26] where TMC is tetra-

(10) Ming, L. J.; Que, L., Jr.; Kriauciunas, A.; Frolik, C. A.; Chen, V. J. *Biochemistry* **1991**, *30*, 11653.
(11) Bill, E.; Bernhardt, F.-H.; Trautwein, A. X.; Winkler, J. H. *Eur. J. Biochem.* **1985**, *147*, 177.
(12) Arciero, D. M.; Lipscomb, J. D.; Huynh, B. H.; Kent, T. A.; Münck, E. *J. Biol. Chem.* **1983**, *258*, 14981.
(13) Enemark, J. H.; Feltham, R. D. *Coord. Chem. Rev.* **1974**, *13*, 339.
(14) Wells, F. V.; McCann, S. W.; Wickman, H. H.; Kessel, S. L.; Hendrickson, D. N.; Feltham, R. D. *Inorg. Chem.* **1982**, *21*, 2306.
(15) Salerno, J. C.; Siedown, J. N. *Biochem. Biophys. Acta* **1979**, *579*, 246.
(16) Pohl, K.; Wieghardt, K.; Nuber, B.; Weiss, J. *J. Chem. Soc., Dalton Trans.* **1987**, 187.
(17) Zhang, Y.; Pavlosky, M. A.; Brown, C. A.; Westre, T. E.; Hedman, B.; Hodgson, K. O.; Solomon, E. I. *J. Am. Chem. Soc.* **1992**, *114*, 9189.
(18) Pavlosky, M. A., Solomon, E. I. Unpublished results.
(19) Hishinuma, Y.; Kaji, R.; Akimoto, H.; Nakajima, F.; Mori, T.; Kamo, T.; Arikawa, Y.; Nozawa, S. *Bull. Chem. Soc. Jpn.* **1979**, *52*, 2863.
(20) Rich, P. R.; Salerno, J. C.; Leigh, J. S.; Bonner, W. D. *FEBS Lett.* **1978**, *93*, 323.
(21) Westre, T. E.; Di Cicco, A.; Filipponi, A.; Natoli, C. R.; Hedman, B.; Solomon, E. I.; Hodgson, K. O. *J. Am. Chem. Soc.* **1994**, *116*, 6757.
(22) Westre, T. E.; Di Cicco, A.; Filipponi, A.; Natoli, C. R.; Hedman, B.; Solomon, E. I.; Hodgson, K. O. *J. Am. Chem. Soc.*, in press.
(23) Co, M. S.; Hendrickson, W. A.; Hodgson, K. O.; Doniach, S. *J. Am. Chem. Soc.* **1983**, *105*, 1144.
(24) Teo, B.-K. *J. Am. Chem. Soc.* **1981**, *103*, 3990.
(25) Hodges, K. D.; Wollman, R. G.; Kessel, S. L.; Hendrickson, D. N.; Van Derveer, D. G.; Barefield, E. K. *J. Am. Chem. Soc.* **1979**, *101*, 906.
(26) Hodges, K. D.; Wollman, R. G.; Barefield, E. K.; Hendrickson, D. N. *Inorg. Chem.* **1977**, *16*, 2746.

methylcyclam, Fe(salen)NO,[27] and Fe(salen)Cl[28] were prepared as described in the literature. With the exception of $[Fe(OH_2)EDTA]^-$, and Fe(salen)Cl, all samples were prepared in an inert atmosphere, *i.e.*, in an anaerobic wet- or drybox or on a Schlenk line. To form an ice crystal-free glass, for the XAS, MCD, and low temperature absorption studies, solution samples were prepared by adding 50% (by volume) glycerol, resulting in samples which were 25 mM in Fe. For Raman isotope perturbations ^{15}NO was purchased from Cambridge Isotope Laboratories. $N^{18}O$ was prepared through the reaction of $H_2{}^{18}O$ (Cambridge) with NO.[29]

Soybean lipoxygenase (SBL) was purified from soybeans (Williams Variety, Tabor Seed Division, Decatur, IL) following published procedures.[30] Enzyme activity was determined by monitoring the absorption of the product formed during the enzymatic reaction at 234 nm ($E_{234} = 2.5 \times 10^4\ M^{-1}\ cm^{-1}$). The specific activity of the final enzyme was ~200 units/mg. To prepare the nitric oxide complex of SBL, the native ferrous enzyme was first treated with an excess of sodium dithionite to remove oxygen and reduce the small amount of ferric contaminant in resting SBL. The enzyme was then anaerobically dialyzed for a few hours to remove sodium dithionite, after which it was anaerobically transferred into a gas tight vial which was filled with N_2 or Ar. Nitric oxide was added to the enzyme using a gas tight syringe. The enzyme and nitric oxide mixture was stirred and incubated for about 15–20 min prior to use. For MCD experiments 50% (v/v) glycerol, which was degassed by freeze–pump–thaw procedures, was added as the glassing agent.

The X-ray absorption spectra were recorded at the Stanford Synchrotron Radiation Laboratory on unfocused beamline 7-3 during dedicated conditions (3 GeV, 25–95 mA). The radiation was monochromatized using a Si(220) double crystal monochromator detuned 50% at 7474 eV to minimize harmonic contamination. An Oxford Instruments continuous-flow liquid helium CF1208 cryostat was used to maintain a constant temperature. Data were measured to $k = 9.5$ $Å^{-1}$ with 1 mm high pre-monochromator beam defining slits. Energies were calibrated using an internal Fe foil standard, assigning the first inflection point to 7111.2 eV.[31] The spectrometer energy resolution was approximately 1.5 eV with a reproducibility of edge position determination of <0.2 eV.

$[Fe(OH_2)EDTA]^{2-}$, $[Fe(OH_2)EDTA]^-$, and FeEDTA–NO solution samples were loaded into 140 μL Lucite EXAFS cells (23 × 2 × 3 mm) with 37 μm Kapton windows and frozen in liquid nitrogen. Data were collected in fluorescence mode at 10 K. The fluorescence signal was collected by an Ar-filled ionization chamber,[32,33] equipped with Soller slits and a Mn filter. $[Fe(TMC)NO](BF_4)_2$, $[Fe(TMC)N_3](BF_4)$, Fe(salen)NO, and Fe(salen)Cl crystalline samples were mixed with BN and ground into a fine powder. The BN/sample mixture was pressed into a 1 mm thick Al spacer that was sealed with 63.5 μm Mylar tape windows and frozen in liquid nitrogen. Data were measured in transmission mode with N_2-filled ionization chambers. Data were measured at 10 K for Fe(salen)Cl, at room temperature for $[Fe(TMC)N_3](BF_4)$, and at 220 K for the $S = 3/2$ forms of Fe(salen)NO and Fe(TMC)NO.

Five to nine scans were averaged for each EDTA solution while two scans were averaged for each powder sample. A smooth pre-edge background was removed from the averaged spectra by fitting a first- or second-order polynomial to the pre-edge region and subtracting this polynomial from the entire spectrum. A one-segment spline of order one was fit to the EXAFS region and the data normalized to an edge jump of one at 7130 eV. The intensities and energies of pre-edge features were quantified by fits to the data. The fitting program EDG_FIT, which utilizes the double precision version of the public domain MINPAK fitting library,[34] was used. EDG_FIT was written by Dr. Graham N. George of the Stanford Synchrotron Radiation Laboratory. All spectra were fit over the range 7108–7118 eV. Pre-edge features were modeled by pseudo-Voigt line shapes (simple sums of Lorentzian and Gaussian functions).[33,35–37] A fixed 50:50 ratio of the Lorentzian to Gaussian contribution for the pre-edge feature successfully reproduced these spectral features. The value reported for the area of a fitted feature was calculated by multiplying the height of the feature by the full width at half-maximum.

UV/vis optical absorption spectra (200–820 nm) at room temperature were recorded on a HP8452A diode array spectrometer. Near-IR (to 2000 nm) and low temperature (77 K) absorption spectra were obtained on a Cary 17 spectrometer interfaced with a Compaq 386 computer. EPR spectra were taken on a Bruker ER220-D-SRC spectrometer with an Air Products model LTR Helitran liquid helium transfer refrigerator. The microwave frequencies were measured with a Hewlett-Packard Model x532B frequency meter.

Magnetic circular dichroism spectroscopy was performed on a Jasco J-500 (200–1100 nm) or J-200 (700–2150 nm) spectropolarimeter equipped with Oxford Instruments SM4-6T and SM4-7T superconducting magnets which are capable of magnetic fields of up to 6.0 and 7.0 T, respectively, and temperatures down to 1.5 K. The depolarization of the samples was checked by measuring the CD of a freshly prepared nickel tartrate solution placed immediately before and after the MCD sample. Samples which exhibited <10% depolarization at 4 K were considered adequate.

Low temperature glass absorption and MCD spectra of protein or model complexes were obtained in a sample cell consisting of two quartz disks sandwiching a 1 or 3 mm thick rubber O-ring spacer. The samples were slowly inserted into the cryostat to reduce the strain of the resulting frozen optical glass. To maintain the structural integrity, mulls of **1** were prepared for absorption and MCD study by grinding the crystals in mineral oil or in poly(dimethylsiloxane) with a mortar in a drybox. The particle size should be smaller than the experimental wavelength of light to limit scattering and depolarization. An optically transparent layer of the resulting mull was sandwiched between two quartz disks.

Magnetic susceptibility measurements were taken in the temperature range 2–260 K on a Quantum Design Model MPMS SQUID magnetometer with the magnetic field up to 5 T. A quartz bucket with silica gel on top, which was flushed thoroughly with argon to remove oxygen, was used as the sample cell for liquid samples. A gas tight syringe was used to inject the solution of **2** through the silica gel, into the bucket anaerobically. The bucket was suspended in the sample holder by a cotton thread, and put into the magnetometer. Background measurements were taken on the same sample bucket used to make the sample of **2**, but filled with the deuterated buffer. This was subtracted from the sample data to correct for diamagnetism. The SQUID measurement on **1** was made with the powder of the complex. The sample was loaded into a gelatin capsule cell in a drybox, and a small cotton ball was placed on top of the powder to prevent spreading upon pumping. A straw was used to hold the cell which was affixed to the magnetometer drive rod. The background measurement was made on the empty cell.

Resonance Raman spectra were taken on a Spex 1403 double monochromator with a cooled RCA C31034A photomultiplier combined with a Spex digital photometer system or a Princeton Applied Research 1462-HR photodiode array. The spectrometer is interfaced with a Compaq 286 computer using a program written in our laboratory for driving the monochromator, data collection, and data analysis. Light sources include a Coherent I-90 K krypton ion laser and a Coherent I-18 UV argon ion laser which was also used to pump Rhodamine 6G and Stilbene 3 dyes in Coherent 590 and 599 lasers. The power of the lasers used was typically 50 mW. Samples were prepared in rubber septum capped Wilmad 528-PP NMR tubes which were purged with

(27) Haller, K. J.; Johnson, P. L.; Feltham, R. D.; Enemark, J. H. *Inorg. Chim. Acta* **1979**, *33*, 119.
(28) Gerloch, M.; Mabbs, F. E. *J. Chem. Soc. A* **1967**, 1598.
(29) Bonner, F. T. *Inorg. Chem.* **1970**, *9*, 190.
(30) Nelson, M. J. *Biochemistry* **1988**, *27*, 4273.
(31) Scott, R. A.; Hahn, J. E.; Doniach, S.; Freeman, H. C.; Hodgson, K. O. *J. Am. Chem. Soc.* **1982**, *104*, 5364.
(32) Stern, E. A.; Heald, S. M. *Rev. Sci. Instrum.* **1979**, *50*, 1579.
(33) Lytle, F. W.; Greegor, R. B.; Sandstrom, D. R.; Marques, E. C.; Wong, J.; Spiro, C. L.; Huffman, G. P.; Huggins, F. E. *Nucl. Instrum. Methods* **1984**, *226*, 542.
(34) Garbow, B. S.; Hillstrom. K. E.; More, J. J. Argonne National Laboratory.
(35) Agarwal, B. K. *X-ray Spectroscopy*; Springer-Verlag: Berlin, 1979; p 276 ff.
(36) Lytle, F. W. In *Applications of Synchrotron Radiation*; Winick, H., Xian, D., Ye, M. H., Huang, T., Eds.; Gordon & Breach: New York, 1989; p 135.
(37) Tyson, T. A.; Roe, A. L.; Frank, P.; Hodgson, K. O.; Hedman, B. *Phys. Rev. B* **1989**, *39*, 6305.

nitrogen or argon. The tubes were spun during data collection using a spinner from a Varian NMR spectrometer. For low temperature resonance Raman measurements, the samples were cooled using a nitrogen flow system, which allowed liquid nitrogen or ice–salt–water–cooled N_2 gas to flow over the samples. Background corrections were made by subtracting the data collected on a blank NMR tube. For resonance Raman enhancement profiles, internal standards, *i.e.*, sodium sulfate or sodium tungstate, were added to calibrate the intensity of the peaks. The program package CART/GMAT/FPERT[38] was used for normal coordinate analyses of the vibrational data. Bond distances and angles were taken from the crystal structure of **1**[16] and the GNXAS analysis for **2**.[21] A general valence force field was used for all calculations.

The 1982 QCPE version of the SCF-Xα-SW program was used for the electronic structure calculations.[39] Three calculations were performed, two on a structure based on **1** with the azides replaced by hydroxides and NH_3 molecules replacing the Me_3TACN nitrogen ligands. One of these calculations was on a linear FeNO unit and the other on a bent FeNO moiety with an FeNO angle of 156°. The third calculation was on a similar structure where the NO has been replaced by O_2. The bond lengths of the non-hydrogen atoms of $[(NH_3)_3(OH)_2FeNO]$, hereafter designated **1′(NO)**, were taken directly from the crystallographic data of **1** and were idealized to pseudo-octahedral coordination with total C_s molecular symmetry. The equatorial ligands bisect the x and y axes, the Fe–NO and Fe–OO bonds are on the z axis, and the NO and OO are bent into the xz plane. The coordinates of $[(NH_3)_3(OH)_2FeO_2]$ hereafter designated **1′(OO)**, were obtained by using the same coordinates as those of **1′(NO)** except for the OO unit. The Fe–OO bond length and bond angle were estimated from heme FeOO complexes: an FeOO angle of 135°, and Fe–O bond length of 1.75 Å, and an OO bond length of 1.25 Å were used.[40,41]

Input parameters, including atomic positions, sphere radii, and α values for **1′(NO)**, linear and bent, and **1′(OO)** can be found in Tables S1A and S1B in the supplementary material. The calculations were considered to have converged when the largest deviation in the potential between iterations was less than 1×10^{-4}. The α values for the atoms were those determined by Schwarz,[42] and those for the inter and outer sphere were weighted by the number of valence electrons. Calculations were performed using averages of Norman radii for the nonmetal atoms.[43] The sphere radii for the metal were increased to 2.7 for these calculations to correct for the tendency of the Norman criteria to overestimate the covalency of the metal ion.[44]

Results and Analysis

(1) X-ray Absorption Spectroscopy. We have compared the Fe K-edge X-ray absorption spectra of $S = 3/2$ $\{FeNO\}^7$ complexes to spectra of ferrous and ferric complexes with similar ligation to elucidate the oxidation state of Fe in the $\{FeNO\}^7$ systems. XAS edge data were collected on complex **2** and compared with data on ferrous and ferric complexes of EDTA. No analogous ferrous or ferric monomeric forms of **1** were available; therefore, the XAS study was extended to two other $S = 3/2$ $\{FeNO\}^7$ complexes, $[Fe(TMC)NO](BF_4)_2$ and Fe(salen)NO, with $[Fe(TMC)N_3](BF_4)$ and Fe(salen)Cl, respectively, as reference complexes. The XAS edge spectra for $[Fe(OH_2)EDTA]^{2-}$, $[Fe(OH_2)EDTA]^-$, and FeEDTA–NO are shown in Figure 1a, $[Fe(TMC)NO](BF_4)_2$ and $[Fe(TMC)N_3](BF_4)$ in Figure 1b, and Fe(salen)NO and Fe(salen)Cl in Figure 1c. The lowest energy transitions are the weak 1s → 3d pre-edge peaks at approximately 7112 eV followed by the 1s → 4p transition at approximately 7123 eV. The 1s → 3d pre-edge region is shown in Figure 1a (inset) for $[Fe(OH_2)EDTA]^{2-}$, $[Fe(OH_2)EDTA]^-$, and FeEDTA–NO, in Figure 1b (inset) for $[Fe(TMC)NO](BF_4)_2$ and $[Fe(TMC)N_3](BF_4)$, and in Figure 1c (inset) for Fe(salen)NO and Fe(salen)Cl. The energies and areas of the pre-edge features were determined by fits to the data and are presented in Table 1. The spectrum of $[Fe(OH_2)EDTA]^{2-}$ has two low intensity pre-edge peaks that are split by 1.9 eV. The $[Fe(TMC)N_3](BF_4)$ data contain an intense feature at 7111.5 eV, with the second derivative of the data (not shown) clearly showing another feature at 7113.4 eV. $[Fe(OH_2)EDTA]^-$, FeEDTA–NO, $[Fe(TMC)NO](BF_4)_2$, Fe(salen)Cl, and Fe(salen)NO all have a single pre-edge peak whose maximum lies between 7112.6 and 7113.0 eV. The pre-edge features of FeEDTA–NO and Fe(salen)NO are more intense than the pre-edge features of $[Fe(OH_2)EDTA]^-$ and Fe(salen)Cl (Figure 1a,c, insets), respectively.

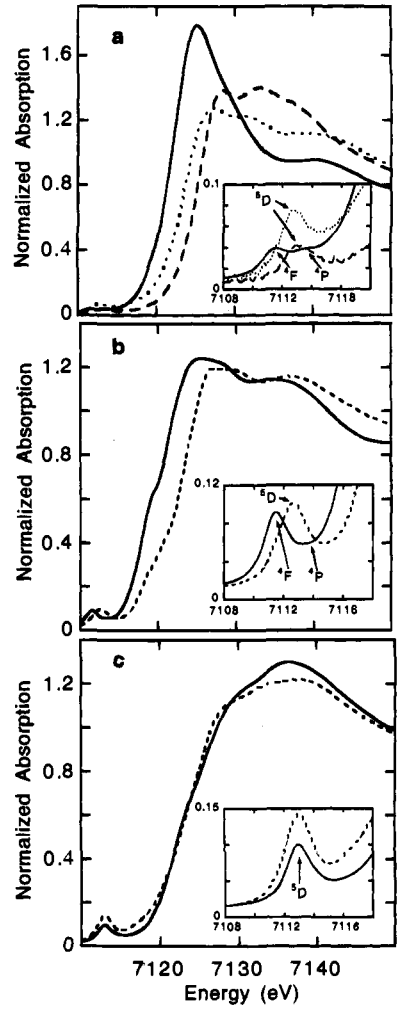

Figure 1. XAS Fe K-edge spectra of (a) $[Fe(OH_2)EDTA]^{2-}$ (—), $[Fe(OH_2)EDTA]^-$ (- - -), and FeEDTA–NO (• • •), (b) $[Fe(TMC)N_3](BF_4)$ (—) and $[Fe(TMC)NO](BF_4)_2$ (- - -), and (c) Fe(salen)Cl (—) and Fe(salen)NO (- - -). Notice the similarity in both the energy of the rising edge and the shape of the edge between $[Fe(OH_2)EDTA]^-$ and FeEDTA–NO in (a) and Fe(salen)NO and Fe(salen)Cl in (c). The insets show the 1s → 3d pre-edge region of the XAS Fe K-edge spectra of (a) $[Fe(OH_2)EDTA]^{2-}$ (—), $[Fe(OH_2)EDTA]^-$ (- - -), and FeEDTA–NO (• • •) (b) $[Fe(TMC)N_3](BF_4)$ (—) and $[Fe(TMC)NO](BF_4)_2$ (- - -), and (c) Fe(salen)Cl (—) and Fe(salen)NO (- - -). Notice that the data in the pre-edge region of the two ferrous complexes, $[Fe(OH_2)EDTA]^{2-}$ and $[Fe(TMC)N_3](BF_4)$, have two features split by ~1.9 eV. The data in the pre-edge region of the ferric complexes, $[Fe(OH_2)EDTA]^-$ and Fe(salen)Cl, and the $\{FeNO\}^7$ complexes, FeEDTA–NO, $Fe(TMC)NO](BF_4)_2$, and Fe(salen)NO, contain a single pre-edge feature.

(38) Fuhres, H.; Karthaa, V. B.; Kidd, K. G.; Krueger, P. J.; Mantsch, H. H. Computer Programs for Infrared Spectroscopy. Bulletin No. 15; National Research Council of Canada, 1976.
(39) Cook, M.; Case, D. A. *QCPE No. 465*, **1991**, *23*, 21.
(40) Momenteau, M.; Reed, C. A. *Chem. Rev.* **1994**, *94*, 659.
(41) Case, D. A.; Huynh, B. H.; Karplus, M. *J. Am. Chem. Soc.* **1979**, *101*, 4433.
(42) Schwarz, K. *Phys. Rev. B* **1972**, *5*, 2466.
(43) Norman, J. G., Jr. *Mol. Phys.* **1976**, *31*, 1191.
(44) Gewirth, A. A.; Cohen, S. L.; Schugar, H. J.; Solomon, E. I. *Inorg. Chem.* **1987**, *26*, 1133.

Table 1. XAS Pre-Edge Energies and Areas for {FeNO}^{7} and Related Complexes

compound	Fe oxidation state	pre-edge energy (eV)	pre-edge area[a] (eV)
$[Fe(H_2O)EDTA]^{2-}$	+2	7111.5, 7113.4	0.038, 0.017
$[Fe(H_2O)EDTA]^{-}$	+3	7112.9	0.067
FeEDTA-NO		7112.8	0.114
$[Fe(TMC)N_3](BF_4)$	+2	7111.5, 7113.4	0.132, 0.007
$[Fe(TMC)NO](BF_4)_2$		7112.6	0.200
Fe(salen)Cl	+3	7113.0	0.132
Fe(salen)NO		7112.9	0.235

[a] The pre-edge area was calculated by multiplying the height of the fitted feature by the full width at half-maximum.

The 1s → 3d pre-edge feature can be used to probe the iron oxidation state in {FeNO}^{7} systems.[17] The 1s → 3d transition is formally electric dipole forbidden, but gains intensity through an allowed quadrupole transition and dominantly by 4p mixing into the 3d states as a result of the noncentrosymmetric environment of the metal site. Because the final state ($1s^13d^{n+1}$) has a different electronic configuration for high spin ferric and high spin ferrous ions, the 1s → 3d feature is sensitive to the oxidation state of the iron site. Two final states of maximum spin multiplicity can be reached in the high spin ferrous case, ^4F and ^4P, while only one state of maximum spin multiplicity can be reached in the high spin ferric case, ^5D. The free ion splitting of the ^4F and ^4P is 2 eV[45] and is readily resolvable at the Fe K-edge. In the ferric case, the ^5D state can split due to ligand field effects into $^5T_2$ and ^5E. Considering that the resolution at the Fe K-edge is ~1.5 eV (12 098 cm^{-1}), the $^5T_2$ and ^5E splitting ($10Dq$) would only be observed in very strong field cases which in fact would result in a low spin complex. The splitting of the pre-edge in $[Fe(OH_2)EDTA]^{2-}$ and $[Fe(TMC)N_3](BF_4)$ is attributed to the ^4F and ^4P free ion splitting of approximately 2 eV. The lack of splitting in the 1s → 3d pre-edge peaks of $[Fe(OH_2)EDTA]^{-}$, FeEDTA–NO, $[Fe(TMC)NO](BF_4)_2$, Fe(salen)Cl, and Fe(salen)NO indicates that the iron in each complex is high spin ferric.

The energy of the edge position (1s → 4p transition) is dependent upon the effective nuclear charge of the absorbing metal atom. The effective nuclear charge of the metal ion is governed by a combination of effects including the formal oxidation state of the metal, the number and type of ligating atoms, and the coordination geometry.[45–50] Therefore, the oxidation state of a metal atom cannot be determined by the edge position without careful consideration of ligation effects on the effective nuclear charge of the metal atom. In the three cases in this study, differences between the types of ligating atoms and the coordination spheres are minimized so that changes in the edge energy can be related to the oxidation state of the iron (Figure 1). The energy of the FeEDTA–NO edge lies between the reduced and oxidized iron–EDTA edges (Figure 1a). However, the FeEDTA–NO spectrum is similar in intensity and shape to the $[Fe(OH_2)EDTA]^{-}$ spectrum. The edge of $[Fe(TMC)NO](BF_4)_2$ is shifted to higher energy than the edge of $[Fe(TMC)N_3](BF_4)$ by ~2 eV (Figure 1b), which is consistent with the difference in oxidation state between ferrous and ferric.[45] The edges of Fe(salen)Cl and Fe(salen)NO (Figure 1c) occur at the same energy, indicating that the iron in each site has the same +3 oxidation state.

In a previous study,[21] iron–ligand bond distances were obtained by EXAFS for $[Fe(OH_2)EDTA]^{2-}$, $[Fe(OH_2)EDTA]^{-}$, and FeEDTA–NO. The first shell bond distances obtained from the $[Fe(OH_2)EDTA]^{-}$ data were 2.04 and 2.34 Å for the Fe–O and Fe–N bonds, respectively. The analogous distances obtained from the $[Fe(OH_2)EDTA]^{2-}$ data were 2.17 and 2.34 Å. The first shell bond distances obtained from the FeEDTA–NO data were 1.76 Å for the Fe–N(O) bond and 2.05 and 2.27 Å for the Fe–O and Fe–N bond distances of the EDTA ligand. The Fe–EDTA bond distances in FeEDTA–NO are more closely matched to the ferric–EDTA bond distances in further experimental support of the ferric oxidation state description.

The XAS edge and pre-edge features as well as the iron–ligand distances obtained from EXAFS data are all consistent and indicate that the Fe in these {FeNO}^{7} complexes is ferric. However, there are quantitative differences in the edge spectra between the ferric reference complexes and the {FeNO}^{7} complexes, giving insight into the geometric and electronic structures of these {FeNO}^{7} complexes. First, the pre-edge feature of the iron–nitrosyl complexes is more intense than that of their ferric counterparts. Empirically, the strength of the pre-edge transition is found to be dependent on the amount of 3d–4p mixing.[48] A distortion of the metal site allows for more 3d–4p mixing, resulting in an increase in the pre-edge intensity since the 1s → 4p transition is electric dipole allowed. This effect is the origin of the increase in the pre-edge intensity of Fe(salen)Cl, which has a square pyramidal geometry, relative to $[Fe(OH_2)EDTA]^{-}$, which has a distorted octahedral geometry. The effect can also be seen in a comparison of $[Fe(OH_2)EDTA]^{2-}$ and $[Fe(TMC)N_3](BF_4)$ where the first pre-edge feature in $[Fe(TMC)N_3](BF_4)$ increased in intensity due to the lowering of symmetry from distorted octahedral to square pyramidal. In the case of FeEDTA–NO, $[Fe(TMC)NO](BF_4)_2$, and Fe(salen)NO complexes, the short Fe–N(O) bond lowers the symmetry around the Fe, resulting in an increase in the intensity of the 1s → 3d pre-edge feature. The second quantitative difference involves the energy of the rising edge, with that of FeEDTA–NO being lower than that of $[Fe(OH_2)EDTA]^{-}$. As has been stated previously, the 1s → 4p transition energy is affected by changes in the effective nuclear charge of the metal atom as well as ligand field effects. In this case, the H_2O of the ferric EDTA complex is replaced by NO^- in FeEDTA–NO. The resulting short Fe–N(O) bond causes a strong axial distortion that splits the 4p levels, with the $4p_z$ orbital shifting to higher energy. Thus, one would expect the 1s → 4p transition to split, with the transition to the $4p_{x,y}$ orbital occurring at approximately the same energy and the transition to the $4p_z$ orbital occurring at higher energy. However, experimentally the FeEDTA–NO edge is at lower energy than the $[Fe(OH_2)EDTA]^{-}$ edge. This shift to lower energy can be explained by charge donation from the NO^- to the ferric center which reduces the effective nuclear charge of the iron and causes the FeEDTA–NO edge to be at a lower energy. Alternatively, in the Fe(salen)Cl and Fe(salen)NO comparison, the edges lie at the same energy. Since Fe(salen)Cl is square pyramidal, the 4p orbitals are split, with the $4p_z$ orbital lying lower in energy. Thus, when the NO^- replaces the Cl^- with a much shorter bond length (1.78 *vs* 2.24 Å), the 1s → $4p_z$ should increase in energy, resulting in an edge shift to higher energy. Experimentally the edges are at the same energy; thus, there must also be charge donation from the NO^-

(45) Shulman, R. G.; Yafet, Y.; Eisenberger, P.; Blumberg, W. E. *Proc. Natl. Acad. Sci. U.S.A.* **1976**, *73*, 1384.
(46) Srivastave, U. C.; Nigam, H. L. *Coord. Chem. Rev.* **1973**, *9*, 275.
(47) Cramer, S. P.; Eccles, T. K.; Kutzler, F. W.; Hodgson, K. O. *J. Am. Chem. Soc.* **1976**, *98*, 1287.
(48) Roe, A. L.; Schneider, D. J.; Mayer, R. L.; Pyrz, J. W.; Widom, J.; Que, L., Jr. *J. Am. Chem. Soc.* **1984**, *106*, 1676.
(49) Wong, J.; Lytle, F. W.; Messmer, R. P.; Maylotte, D. H. *Phys. Rev. B* **1984**, *30*, 5596.
(50) Kau, L. S.; Spira-Solomon, D. J.; Penner-Hahn, J. E.; Hodgson, K. O.; Solomon, E. I. *J. Am. Chem. Soc.* **1987**, *109*, 6433.

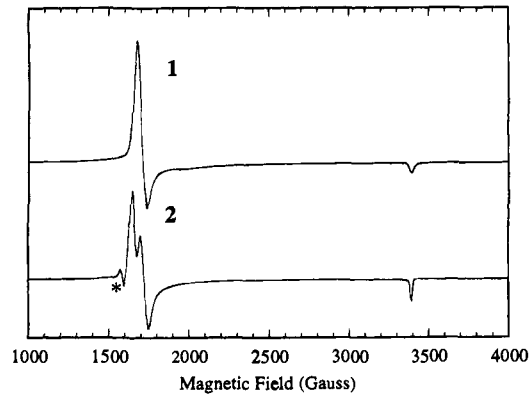

Figure 2. EPR spectra at $T = 5$ K of complex **1** in methanol and complex **2** in 0.1 M phosphate buffer, pH 6, with 50% (v/v) glycerol. The asterisk indicates adventitious Fe^{3+} at $g = 4.3$. EPR parameters are the following: microwave frequency, 9.52 GHz; power, 10 mW; modulation amplitude, 10 G.

to the ferric center of the salen complex, reducing the effective nuclear charge of the iron.

In summary, both the energy of the rising edge and the shape of the edge of the $\{FeNO\}^7$ complexes are similar to those of the ferric complexes with corresponding ligation (*i.e.*, $[Fe(OH_2)EDTA]^-$ *vs* FeEDTA−NO and Fe(salen)Cl *vs* Fe(salen)NO, Figure 1a,c, respectively). All three of the $\{FeNO\}^7$ complexes exhibit a single, intense pre-edge feature which is consistent with a ferric complex that has a distorted iron site. In the $\{FeNO\}^7$ complexes, the short Fe−N(O) bond of ~1.7 Å provides a strong axial distortion of the iron active site. The bond distances obtained from EXAFS data of $[Fe(OH_2)EDTA]^{2-}$, $[Fe(OH_2)EDTA]^-$, and FeEDTA−NO show that the Fe−EDTA distances of FeEDTA−NO are much more similar to the distances in $[Fe(OH_2)EDTA]^-$ than in $[Fe(OH_2)EDTA]^{2-}$.[21] On a quantitative level the rising edge of FeEDTA−NO is shifted by 2 eV to lower energy relative to $[Fe(OH_2)EDTA]^-$ consistent with significant charge donation from the NO^- ligand to the Fe^{3+} center.

(2) EPR and Magnetic Susceptibility. The ground state properties of **1** and **2** were studied by EPR spectroscopy and SQUID magnetic susceptibility measurements. Figure 2 shows the EPR spectra of **1** and **2** in frozen solution. Both systems exhibit typical $S = 3/2$ ground state EPR with g values of 2 and 4. A control experiment was performed on NO gas dissolved in buffer which shows a large positive signal at $g = 2$; therefore, the negative $g = 2$ signals in the spectra in Figure 2 clearly arise from the $\{FeNO\}^7$ complexes. While the spectrum of **1** (Figure 2) has a single peak at $g = 4.0$, complex **2** (Figure 2) shows a splitting with $g = 3.9$ and $g = 4.1$, which is consistent with published results.[7] The observed EPR spectra of the $S = 3/2$ complexes can be described with a spin Hamiltonian (eq 1), where $g_o = 2.0$ and D and E are the axial

$$H = D[S_z^2 - S(S+1)/3] - E(S_x^2 - S_y^2) + g_o\beta SH \quad (1)$$

and rhombic zero-field splitting parameters, respectively. In the case of axial complexes ($E/D \sim 0$), this Hamiltonian generates two doublets, $M_s = \pm 1/2, \pm 3/2$, split by $2D$. The EPR signals arise from the $\pm 1/2$ doublet which is lowest in energy for a positive D, with $g_{\parallel} = 2.0$ and $g_{\perp} = 4.0$. As the system deviates from the ideal axial limit ($E/D > 0$), the $g_{\perp}$ signal will split in field, which provides an estimate of the E/D ratio. From the ground state effective g values, it has been determined that E/D is 0.016 for **2** and ~0 for **1**.

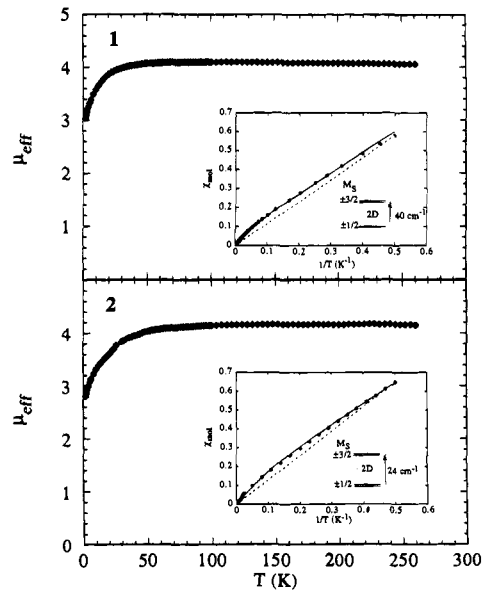

Figure 3. Effective magnetic moments of the complexes **1** and **2**. μ_{eff} is calculated to be $\mu_{eff} = 2.828(\chi T)^{1/2}$. The temperature range is 2−260 K at 2000 G. The insets show the magnetic susceptibility of complexes **1** and **2**. χ_{mol} is the molar susceptibility. Solid circles are the experimental data measured by SQUID. Dashed lines indicate the ideal Curie behavior. The solid lines represent the best fit to the experimental data using eq 2. Zero-field splitting parameters obtained are $g = +2.0$, and $D = +20 \pm 2$ cm^{-1} for complex **1** and $g = 2.0$ and $D = +12 \pm 1$ cm^{-1} for complex **2**.

Figure 3 gives the magnetic susceptibility data, over the temperature range of 2−260 K, for **1** (top) and **2** (bottom). Both complexes exhibit a constant effective magnetic moment, μ_{eff}, from 260 K down to approximately 50 K, where μ_{eff} starts to decrease. At 260 K, μ_{eff} is determined to be 4.16 for **2** and 4.05 for **1**. The latter is consistent with the value of 4.06 at 293 K reported for **1** in the literature.[16] While most structurally defined $\{FeNO\}^7$ systems show $S = 1/2$ to $S = 3/2$ spin crossover with a system dependent transition temperature ranging from 80 to 180 K,[13,14,17] the magnetic susceptibilities of **1** and **2** show that both molecules are in the pure $S = 3/2$ spin state throughout a wide temperature range, which allows the application of a wide range of spectroscopic techniques. These two non-spin-crossover $\{FeNO\}^7$ molecules are therefore ideal for investigating the origin of the $S = 3/2$ state and generally understanding the electronic structure description.

The decrease in μ_{eff} below 50 K is due to zero-field splitting of the system. Magnetic measurements at variable temperatures can be used to determine the zero-field splitting. As shown in Figure 3 (insets), where experimental molar magnetic moments, χ_{mol} (solid circle), of **1** (top) and **2** (bottom) are plotted against $1/T$, the experimental data do not follow Curie law behavior (dashed line). It also can be observed from Figure 3 that μ_{eff} starts to decrease at about 50 K, indicating the depopulation of the $M_s = \pm 3/2$ sublevels. Note that throughout the range of 50−260 K no increase in μ_{eff} is observed, indicating no thermal population of higher spin states (*i.e.*, $S_{total} = 5/2$ or $7/2$ *vide infra*).

Magnetic properties of these isolated spin multiplet systems are described with the effective spin Hamiltonian given in eq 1. Given these energy levels, the magnetic susceptibility can be calculated by applying the Van Vleck equation[51] to the $S = 3/2$ system, which is given by eq 2, $\chi_{\parallel}$ and $\chi_{\perp}$ are the magnetic

(51) Van Vleck, J. H. *The Theory of Electric and Magnetic Susceptibilities*; Oxford University Press: Oxford, 1932; Chapter XII.

$$\chi_{\parallel} = \frac{N\beta^2 g^2}{4kT}\left[\frac{\frac{\sinh(y/2)}{y/2} + 9e^{-x}\frac{\sinh(3y/2)}{(3y/2)}}{\cosh(y/2) + e^{-x}\cosh(3y/2)}\right]$$

$$\chi_{\perp} = \frac{N\beta^2 g^2}{4kT}\left[\frac{\frac{\sinh(y)}{y} + \frac{3}{2x}\cosh(y)e^{z} - \frac{3}{2x}e^{-z}e^{-x}}{e^{z}\cosh(y) + e^{-z}e^{-x}}\right] \quad (2)$$

$$\bar{\chi} = \frac{\chi_{\parallel} + 2\chi_{\perp}}{3}$$

susceptibility when the external magnetic field is parallel and perpendicular to the molecular z axis, respectively, and $\bar{\chi}$ is the average magnetic susceptibility for a solution or powder sample. Using eq 2 to simulate the experimental susceptibility data for both complexes, the solid lines in Figure 3 (insets) were produced, which represent the best fit to the data. Zero-field splitting parameters, $D = +12 \pm 1$ cm^{-1} for **2** and $D = +20 \pm 2$ cm^{-1} for **1**, are obtained. For **2**, the D value obtained is comparable to previously reported $D = +19 \pm 1$ cm^{-1} from EPR[52] and in good agreement with the $D = +12 \pm 1$ cm^{-1} from Mössbauer spectroscopy.[12]

EPR and magnetic susceptibility measurements demonstrate that both **1** and **2** are in a pure $S = 3/2$ state with no spin crossover in the temperature range of 2–260 K and no population of higher total spin states at 260 K. They have positive zero-field splittings with the $M_s = \pm 1/2$ sublevels lowest in energy. Both systems exhibit axial EPR spectra with $g_{\parallel} = 2.0$, $g_{\perp} \approx 4$, and E/D ratios of less than 0.02.

(3) Resonance Raman Spectroscopy. The resonance Raman spectra of **1** and **2** have been obtained with $^{14}N^{16}O$, $^{15}N^{16}O$, and $^{14}N^{18}O$ isotropic perturbations (Figures 4 and 5). **1** shows three isotope sensitive vibrations (Figure 4). In the metal–ligand region, the peaks at 497 and 436 cm^{-1} shift to 489 and 435 cm^{-1}, respectively, upon $^{15}N^{16}O$ substitution, and to 490 and 434 cm^{-1}, respectively, upon $^{14}N^{18}O$ substitution. An additional peak at 482 cm^{-1} is observed, which does not shift upon isotope substitution. The intraligand region shows ν(NO) at 1712 cm^{-1}, which shifts to 1681 and 1672 cm^{-1} upon $^{15}N^{16}O$ and $^{14}N^{18}O$ substitution, respectively. This value for ν(NO) is slightly larger than that reported from an IR spectrum of **1** in a methanol solution.[16] For **2**, three features (Figure 5) also shift upon isotropic substitution of NO. The metal–ligand region shows a complex feature centered at 496 cm^{-1}. Gaussian resolution of this feature indicates that the peak at 496 cm^{-1} and the shoulder at 517 cm^{-1} shift to 490 and 515 cm^{-1}, respectively, upon $^{15}N^{16}O$ substitution, and to 491 and 513 cm^{-1}, respectively, upon $^{14}N^{18}O$ substitution, while the shoulder at 468 cm^{-1} is unaffected by isotope substitution. The intraligand region shows an isotope sensitive peak at 1776 cm^{-1}, assigned as ν(NO), which shifts to 1744 and 1737 cm^{-1} upon $^{15}N^{16}O$ and $^{14}N^{18}O$ substitution, respectively. In metal–nitrosyl complexes δ(MNO) has been found to exhibit a larger (6–15 cm^{-1}) ^{15}N isotope shift than ν(MN) (1–6 cm^{-1}).[53,54] Therefore, we assign the 498 cm^{-1} peak of **1** as δ(FeNO), and the vibration at 436 cm^{-1} as ν(FeN). Similarly we assign the 496 cm^{-1} vibration of **2** as δ(FeNO), and the 517 cm^{-1} vibration as ν(FeN). Resonance Raman excitation profiles have been obtained for both complexes and will be presented in a following section.

We have performed normal coordinate calculations using a general valence force field on the Fe–N–O unit for **1** and **2**;

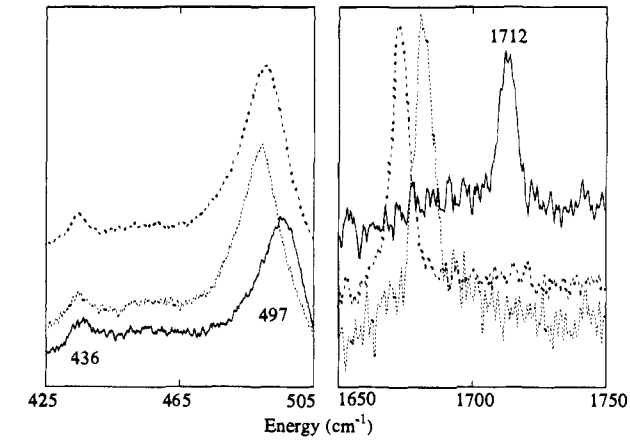

Figure 4. Resonance Raman spectra of NO isotope substituted complex **1** (excitation wavelength 520.8 nm, power 50 mW): $^{14}N^{16}O$ (—), $^{15}N^{16}O$ (- - -), $^{14}N^{18}O$ (— — —).

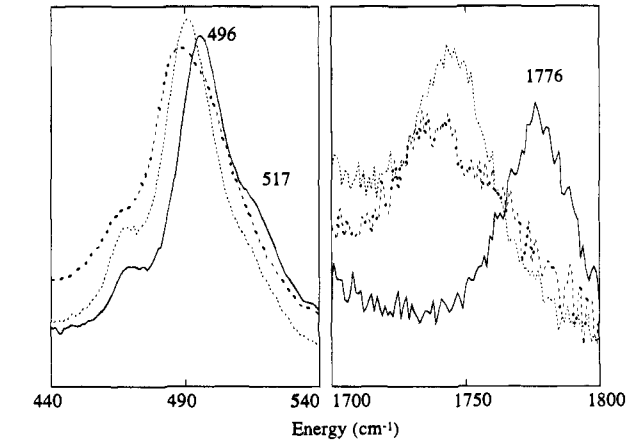

Figure 5. Resonance Raman spectra of NO isotope substituted complex **2** (excitation wavelength 457.9 nm, power 50 mW): $^{14}N^{16}O$ (—), $^{15}N^{16}O$ (- - -), $^{14}N^{18}O$ (— — —).

the results are summarized in Table 2. The applicability of using a simple three-body model in normal coordinate calculations of the MNO unit has been shown in the literature.[53,54] The NO stretching force constants determined from normal coordinate calculations for complexes **1** and **2** are 12.6 and 13.2 mdyn/Å, respectively. To obtain an initial experimental estimate of the charge on the NO for **1** and **2**, the intraligand stretch f(NO) force constants have been calculated using existing vibrational data on representative diatomic NO species: NO^+, NO^0, and NO^-. Values of ν(NO) are as follows: NO^- from ionic CsNO,[55] 1346 cm^{-1}; NO^0 from NO gas,[56] 1876 cm^{-1}; NO^+ from, *e.g.*, ionic $NOBF_4$,[57] 2150 cm^{-1}. The calculated f(NO) values for these diatomics are 8.4, 15.5, and 21.3 mdyn/Å, respectively. The experimental f(NO) values for **1** and **2** fall between those of NO^0 and NO^-, and thus consistent with the XAS results the NO has been partially reduced. It should be noted here and will be expanded upon later that charge transfer from Fe to NO is into a π^* orbital while charge donation from the resulting NO^- to the Fe^{3+} dominantly involves a σ^* orbital which will be more effective at strengthening the NO bond (*vide infra*). Comparison of the two complexes show that both ν(NO) and ν(FeN) and the corresponding force constants are higher in complex **2** than in complex **1**, indicating that more

(52) Bonner, W. D.; Blum, H.; Rich, P. R.; Salerno, J. C. *Frontiers of Biological Energetics*; Academic Press: New York, 1978; Vol. II, p 997.
(53) Miki, E.; Mizumachi, K.; Ishimoro, T.; Okuno, H. *Bull. Chem. Soc. Jpn.* **1973**, *46*, 3779.
(54) Quinby-Hunt, M.; Feltham, R. D. *Inorg. Chem.* **1978**, *17*, 2515.
(55) Tevault, D. E.; Andres, L. *J. Phys. Chem.* **1973**, *77*, 1646.
(56) Nakamoto, K. *Infrared and Raman Spectra of Inorganic and Coordination Compounds*, 3rd ed.; Wiley: New York, 1978; p 295.
(57) Cotton, F. A.; Wilkinson, G. *Advanced Inorganic Chemistry*, 5th ed.; Wiley: New York, 1988; p 322.

Table 2. Normal Coordinate Calculations

		ν(NO)		ν(FeN)		δ(FeNO)		calcd force constants[a] (mdyn/Å)		
		obsd	calcd	obsd	calcd	obsd	calcd			
complex **1**	$^{14}N^{16}O$	1712	1713	436	439	497	498	$f_{11} = 12.6$	$f_{12} = 0.3$	$f_{13} = 0.2$
	$^{15}N^{16}O$	1681	1680	435	433	489	489		$f_{22} = 2.7$	$f_{23} = 1.5$
	$^{14}N^{18}O$	1672	1672	434	431	490	490			$f_{33} = 0.8$
complex **2**	$^{14}N^{16}O$	1776	1777	517	520	496	498	$f_{11} = 13.2$	$f_{12} = 0.3$	$f_{13} = 0.1$
	$^{15}N^{16}O$	1744	1743	515	514	490	489		$f_{22} = 3.2$	$f_{23} = 1.6$
	$^{14}N^{18}O$	1737	1736	512	512	491	489			$f_{33} = 1.0$

[a] Key: f_{11}, force constant of NO stretch; f_{12}, Fe−N stretch and NO stretch interaction force constant; f_{13} Fe−NO bend and NO stretch interaction force constant; f_{22}, force constant of Fe−N stretch; f_{23}, Fe−N stretch and Fe−NO bend interaction force constant; f_{33}, force constant of Fe−NO bend.

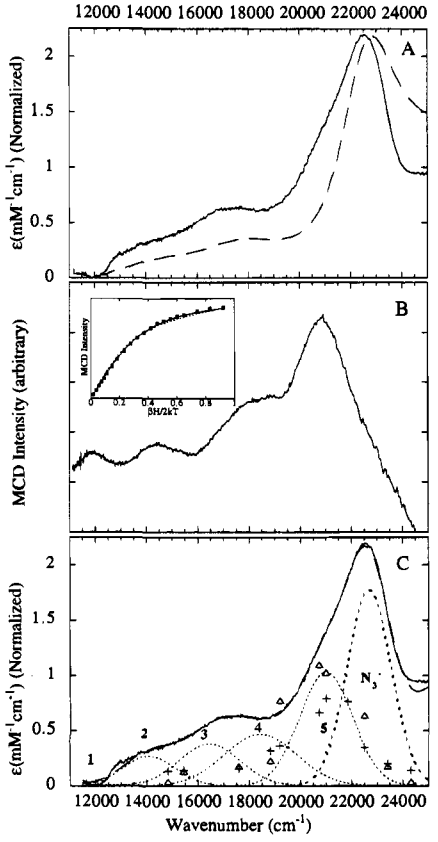

Figure 6. Low temperature (100 K) absorption (A), MCD (90 K and 5 T) mull spectra (B), and resonance Raman excitation profiles and Gaussian resolution (C) for complex **1**. In (A), the solid line is from a mull of **1** while the broken line is from an ethanol solution. In (C), the triangles represent the excitation profile of the δ(FeNO) of 497 cm^{-1}, while the crosses represent the excitation profile of the ν(NO) of 1712 cm^{-1}. The inset in (B) shows the saturation magnetization data for band 5 at 1.8 K (squares), the theoretical fit with $M_z/M_{xy} = 0$ (—), and the fit with $M_z/M_{xy} = 100$ (- - -).

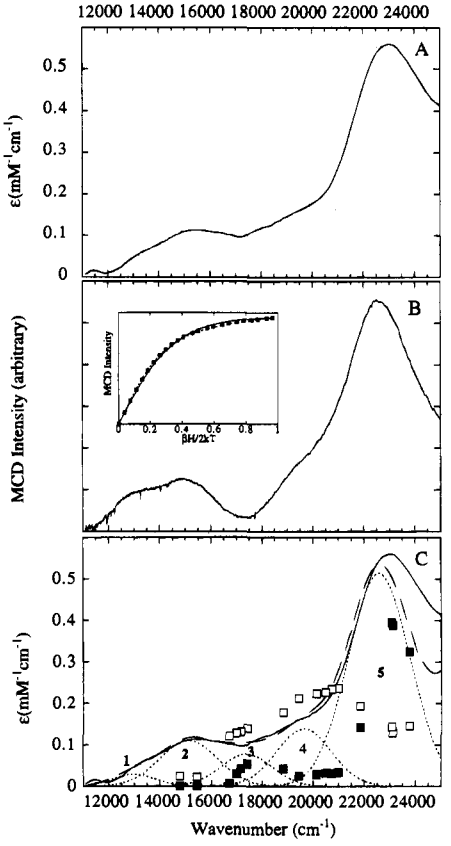

Figure 7. Low temperature (77 K) absorption (A), MCD (90 K and 3 T) spectra (B), and resonance Raman excitation profiles and Gaussian resolution (C) for complex **2**. In (C), the nonfilled squares represent the excitation profile of the δ(FeNO) of 496 cm^{-1}, while the filled squares represent the excitation profile of the ν(NO) of 1776 cm^{-1}. The inset in (B) shows the saturation magnetization data for band 5 at 1.8 K (squares), the theoretical fit with $M_z/M_{xy} = 0$ (—), and the fit with $M_z/M_{xy} = 100$ (- - -).

electron density has been donated from the NO to the iron, strengthening the NO and FeN bonds in complex **2**.

(4) Absorption, MCD, and Resonance Raman Profiles. Figures 6 and 7 show the low temperature absorption and MCD spectra and the resonance Raman excitation profiles of **1** and **2**, respectively, in the energy range of 11000−25000 cm^{-1}. Gaussian resolutions for the absorption spectra are presented in Figures 6C and 7C. Lower energy (5000−10000 cm^{-1}) absorption and MCD spectra were obtained on both complexes with no transitions observed.[18]

Low temperature (~100 K) absorption and MCD spectra of **1** are presented in Figure 6A,B. The solid line in Figure 6A is taken from an ethanol solution of **1**; the broken line is from the mull sample. Both spectra look qualitatively similar with variations in relative intensities, which indicates the structure does not change in solution. An intense band at 22 750 cm^{-1}, with an experimental extinction coefficient of $\epsilon = 2100$ M^{-1} cm^{-1}, dominates the absorption spectrum, while a number of broad features are also present at lower energy. In contrast, the MCD spectrum (Figure 6B) of **1** does not exhibit the 22 750 cm^{-1} band. Instead, the most intense band in the MCD spectrum is centered at 21 000 cm^{-1} with three resolvable bands to the lower energy side, one at ~18 400 cm^{-1}, and two overlapping features at 14 300 and 11 700 cm^{-1}. Absorption and MCD data together require that at least six transitions are present. Gaussian resolution of these bands, for the best fit to the absorption spectrum, is presented in Figure 6C, and the energy and intensity of each transition are listed in Table 3. These transitions are numbered in Figure 6C. Note that the evidence for band 1 comes from the MCD spectrum in Figure 6B. The most intense band is at 22 750 cm^{-1} ($\epsilon = 1840$ M^{-1} cm^{-1}); however, this band is not included in Table 3 since our

Table 3. Energies and Intensities of Absorption Bands for **1** and **2**

band number	energy (cm^{-1})	ϵ (M^{-1} cm^{-1})
	Complex **1**	
1	11 700	15
2	14 100	284
3	16 450	400
4	18 440	490
5	21 000	1085
	Complex **2**	
1	12 900	28
2	15 120	110
3	17 400	77
4	19 650	138
5	22 580	550

resonance Raman studies show that an N_3^-–Fe^{3+} vibration at 482 cm^{-1} is in resonance with this band, which indicates this band is an $N_3^- \rightarrow Fe^{3+}$ CT transition.[18] Resonance Raman excitation profiles for FeNO vibrations have also been obtained for **1** and are included in Figure 6C. The ν(NO) at 1712 cm^{-1} is in resonance with absorption bands 3–5. The δ(FeNO) at 497 cm^{-1} is also in resonance with absorption bands 3–5. The ν(FeN) at 436 cm^{-1} is weak and only observable using excitation energies of 19 500 ± 500 cm^{-1}, showing that it is weakly resonance enhanced by bands 4 and 5.

Complex **2** exhibits one intense band at ~23 000 cm^{-1} with an extinction coefficient of ϵ = ~580 M^{-1} cm^{-1} and one weaker band at ~15 000 cm^{-1} (ϵ = ~120 M^{-1} cm^{-1}) in both absorption and MCD spectra, as shown in Figure 7A,B. Shoulders, which are better resolved in the MCD spectrum in Figure 7B, are also present in both spectra at ~19 000 and ~13 000 cm^{-1}. Although MCD intensity reaches a minimum around 17 400 cm^{-1}, the absorption spectrum clearly exhibits intensity in this region, indicating the presence of an additional band. The existence of this band is also supported by resonance Raman profile data (see below). The Gaussian resolution shown in Figure 7C is the best fit to the absorption spectrum; the energy and extinction coefficient for each band are listed in Table 3. For complex **2**, the ν(NO) at 1776 cm^{-1} is in resonance with absorption bands 3 and 5. The δ(FeNO) at 496 cm^{-1} is greatly resonance enhanced by absorption bands 3 and 4 and goes down in intensity under the strongest absorption band 5. The ν(MN) is not strongly enhanced by any of the transitions; however, δ(FeNO) is so intensely enhanced by bands 3 and 4 that small changes in the relative intensity of ν(MN) may not have been detected.

Saturation magnetization data for bands 2 and 5 were taken at 1.8 K for fields of 0–5.5 T for complexes **1** and **2**. The saturation curves for band 5, which are superimposable with the curves for band 2 in complexes **1** and **2**, are shown in the insets of Figures 6B and 7B. These curves have been fit to an equation[58] for a randomly oriented system (*e.g.*, frozen glass and mull samples) with axial symmetry and an isolated Kramer's doublet ground state, allowing for a linear B term and a range of polarization ratios of M_z/M_{xy} = 0–100. The fits, with the limiting polarization ratios, are included in the insets, and it is found that, on the basis of the presence of a large B term contribution, these data do not allow a quantitative estimate of this polarization ratio.

Qualitatively, the MCD and absorption spectra and the resonance Raman profiles of **1** and **2** are extremely similar, as expected, since they are both bent complexes with an FeNO angle of 156°. Their absorption spectra have each been fit with five bands associated with the FeNO unit which are listed in Table 3. Both complexes exhibit a set of two bands at a higher energy region with larger intensities. At lower energy, there are a group of three weaker bands. This spectral similarity indicates parallel electronic structures in these complexes. Quantitatively, the energies of the transitions shift between two complexes. Transitions in complex **2** all appear at higher energies relative to their corresponding bands in **1**; *e.g.*, band 5 is ~1600 cm^{-1} higher in energy in **2** compared to **1**. In addition, the relative intensities of the bands are also different, with those of complex **1** being more intense. The resonance Raman excitation profiles for both complexes show enhancements of the FeNO vibrations by bands 3–5. The profile for complex **2** is of higher resolution than for complex **1** and clearly shows that bands 3 and 4 strongly enhance the Fe–NO bend and enhancement of both the bend (with reduced intensity) and the NO stretch by the highest intensity absorption band 5.

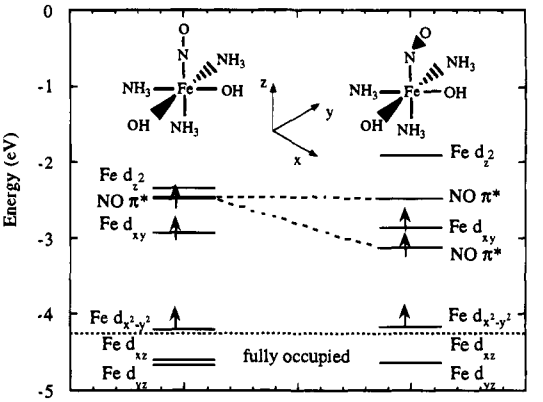

Figure 8. Energy level diagrams for spin restricted calculations on **1′(NO)** with both a linear (left) and bent (right) FeNO unit. Arrows indicate the three unpaired electrons in each calculation. Shown at the top are the core atoms and coordinate frame for **1′(NO)**. The molecular coordinate frame has z along the Fe–NO.

(5) SCF-Xα-SW. In order to gain further insight into the electronic structure of Fe–NO complexes and as a complement to experimental results, SCF-Xα-SW calculations were performed on structure **1′**, based on the crystal structure of **1**. In the calculations on **1′(NO)**, both linear and bent (156°) FeNO units were considered. While not appropriate for complexes with unpaired electrons, spin restricted calculations were first performed in order to compare them with existing spin restricted bonding descriptions in the literature. Spin unrestricted calculations are presented next. These are related to experimental data, and a quantitative description of the electronic structure is developed. These spin unrestricted calculations are then used to assign the absorption and MCD spectra of these complexes. Finally these results are extended to develop a bonding description of potential $\{FeO_2\}^8$ intermediates, which would be generated by reaction of O_2 with the starting ferrous complex, by considering the calculation on **1′(OO)** where the NO is replaced by O_2.

(a) Spin Restricted Calculations on Linear and Bent 1′(NO) Complexes. In the description of the spin restricted calculations of **1′(NO)**, emphasis will be placed on the valence d orbitals and π^* orbitals of the NO. The spin state in the calculations was fixed at S = 3/2, and a molecular symmetry of C_s was used. Since earlier literature relates electronic structure to the FeNO angle, *i.e.*, whether the complex is linear or bent, both linear and bent (FeNO angle of 156°) structures were considered, Figure 8 (top). In these calculations, all parameters were kept equal except for the Fe–NO angle; *i.e.*,

(58) (a) Schatz, P. N.; Mowery, R. L.; Krausz, E. R. *Mol. Phys.* **1978**, *35*, 1537. (b) McCormick, J. M.; Reem, R. C.; Solomon, E. I. *J. Am. Chem. Soc.* **1991**, *113*, 9066.

Table 4. Charge Decomposition of the Spin Restricted Linear Calculation on **1′(NO)**

															% for Fe		
level	occup	orbital	energy (eV)	Fe	N1 (NO)	N2	N3	O1 (OH)	O2 (NO)	H1	H2	H3	H4	H5	H6	s	p	d
19A′	0.0	d_{z^2}	−2.352	68	7	9	9	2	3	1	0	0	0	0	0	2	2	97
13A″	0.0	NOπ*	−2.461	28	49	3	0	1	20	0	0	0	0	0	0	0	5	95
18A′	1.0	NOπ*	−2.484	33	44	0	1	2	18	1	0	0	0	0	0	1	5	94
12A″	1.0	d_{xy}	−2.936	71	1	17	0	6	0	3	0	0	0	0	0	0	0	100
17A′	1.0	$d_{x^2-y^2}$	−4.195	72	0	1	0	27	0	0	0	0	0	0	0	0	0	100
11A″	2.0	"d_{yz}"	−4.610	36	7	0	0	52	5	0	0	0	0	0	0	0	0	100
16A′	2.0	"d_{xz}"	−4.667	37	7	1	3	46	5	0	0	0	0	0	0	0	0	100
15A′	2.0	"d_{xz}"	−6.028	40	4	1	13	33	7	0	0	2	0	0	0	1	3	96
9A″	2.0	"d_{yz}"	−6.083	42	4	2	0	44	7	0	0	1	0	0	0	0	0	100

Table 5. Charge Decomposition of the Spin Restricted Bent Calculation on **1′(NO)**

															% for Fe		
level	occup	orbital	energy (eV)	Fe	N1 (NO)	N2	N3	O1 (OH)	O2 (NO)	H1	H2	H3	H4	H5	H6	s	p	d
19A′	0.0	d_{z^2}	−1.909	64	15	4	6	4	6	2	0	0	0	0	0	4	5	91
13A″	0.0	NO π*	−2.482	29	46	4	0	0	19	0	0	0	0	0	0	0	4	96
12A″	1.0	d_{xy}	−2.869	71	1	17	0	6	1	3	0	0	0	0	0	0	1	99
18A′	1.0	NO π*	−3.133	45	30	6	4	1	14	0	0	0	0	0	0	0	2	97
17A′	1.0	$d_{x^2-y^2}$	−4.160	73	0	1	0	26	0	0	0	0	0	0	0	0	0	100
11A″	2.0	d_{yz} + OH	−4.639	37	8	0	0	49	6	0	0	0	0	0	0	0	0	100
16A′	2.0	d_{xz} + OH	−4.643	35	9	1	7	40	6	0	0	0	0	0	0	0	2	97
9A″	2.0	OH + d_{yz}	−6.038	39	3	2	0	47	7	0	0	1	0	0	0	0	0	100
15A′	2.0	OH + d_{xz}	−6.050	38	5	1	8	37	9	0	0	1	0	0	0	2	1	97

the Fe−N and N−O bond lengths were fixed at 1.738 and 1.142 Å, respectively.

The charge breakdown of the Fe d orbitals and NO π* orbitals for the linear spin restricted calculation on **1′(NO)** is given in Table 4. The associated energy level diagram is given in Figure 8 (left). The two NO π* levels, 13A″ and 18A′, are close in energy, but only one contains an electron. This corresponds to a neutral NO^0. There are six electrons in the Fe d orbitals, leading to a nominally ferrous (d^6) complex. Since the Fe d_{z^2} orbital, level 19A′, is unoccupied (it is at high energy due to the strong axial Fe−NO bond), the Fe(II) can best be described as an intermediate spin $S = 1$ ion. The two unpaired Fe d electrons reside in the Fe d_{xy} and Fe $d_{x^2-y^2}$ orbitals, levels 12A″ and 17A′ in Table 4.[59] The d_π orbitals, d_{xz} and d_{yz}, are both fully occupied. Note that the Fe d_{xz} and d_{yz} orbitals mix with hydroxo ligand based orbitals at similar energies which leads to pairs of orbitals which have almost equal amounts of Fe character (levels 16A′ and 15A′ involve d_{xz} while levels 11A″ and 9A″ involve d_{yz} orbitals). For simplicity only the highest energy orbitals are included in Figure 8. In summary, this spin restricted calculation for the linear **1′(NO)** complex can be considered as an intermediate spin $S = 1$ d^6 iron ferromagnetically coupled to an $S = 1/2$ NO^0 to produce the $S = 3/2$ ground state.

The spin restricted bent **1′(NO)** complex has a similar electronic structure description. The charge decompositions of the Fe d and NO π* orbitals are listed in Table 5 and shown in Figure 8 (right). Again only one of the NO π* orbitals contains an electron and the species can be considered as NO^0. A main difference between this calculation and the linear calculation is that the occupied in-plane (the FeNO plane) NO π* orbital, 18A′, has been significantly stabilized below the unoccupied out-of-plane NO π* orbital, level 13A″, due to the loss of the strong Fe−N−O π antibonding which is maximized in the linear structure. The splitting is given by the dashed lines in Figure 8. The d orbital description is essentially the same. The Fe d_{z^2} orbital, level 19A′, is unoccupied, the Fe d_{xy} and Fe $d_{x^2-y^2}$ orbitals, levels 12A″ and 17A′, are both half-occupied, and the d_π orbitals are both fully occupied. Analogous to the linear case, the d_π orbitals, d_{xz} and d_{yz}, mix with hydroxide based ligand orbitals, leading to orbitals which are a mixture of Fe d_{yz}, Fe d_{xz}, and hydroxide (Table 5, levels 15A′, 16A′, 9A″, and 11A″). The bent **1′(NO)** can also be described as an intermediate spin $S = 1$ d^6 iron ferromagnetically coupled to an $S = 1/2$ NO^0 to obtain the $S = 3/2$ ground state.

While these spin restricted calculations do not accurately allow for exchange effects in open shell species, it is useful to compare these calculations to existing qualitative descriptions of iron−nitrosyl bonding, since these are normally spin restricted in nature. The above calculations show a clear preference for the bent structure over the linear structure with the stabilization of the half-occupied in-plane NO π* orbital. This is consistent with the qualitative bonding description put forth by Feltham and Enemark and others.[13,60]

(b) Spin Unrestricted Calculations on Linear and Bent 1′(NO) Complexes. In order to accurately portray the bonding in open shell species, spin unrestricted calculations should be performed. These calculations allow spin up and spin down electrons to occupy different spatial orbitals and are accomplished easily in the SCF-Xα-SW formalism.[61] For iron complexes in particular, these calculations have been shown to reproduce experimental observables.[62−66]

Since this analysis will probe NO bonding in the FeNO unit, it will be useful to refer to the bonding description for the free molecule. An energy level diagram obtained from SCF-Xα-SW calculations on NO (bond length 1.15 Å, Norman radii)

(59) Since the equatorial ligands bisect the coordinate axes, the Fe d_{xy} and Fe $d_{x^2-y^2}$ levels are reversed compared to their normal description; *i.e.*, Fe d_{xy} is now part of the e_g set of O_h d orbitals.

(60) Hoffman, R.; Chen, M. M. L.; Elian, M.; Rossi, A.; Mingos, D. M. P. *Inorg. Chem.* **1974**, *13*, 2666.
(61) Slater, J. C. *Quantum Theory of Molecules and Solids*; McGraw Hill: New York, 1974.
(62) Brown, C. A.; Remar, G. J.; Musselman, R. L.; Solomon, E. I. *Inorg. Chem.*, in press.
(63) Butcher, K. D.; Didziulis, S. V.; Briat, B.; Solomon, E. I. *J. Am. Chem. Soc.* **1990**, *112*, 2231.
(64) Butcher, K. D.; Gebhard, M. S.; Solomon, E. I. *Inorg. Chem.* **1990**, *29*, 2067.
(65) Noodleman, L.; Baerands, E. J. *J. Am. Chem. Soc.* **1984**, *106*, 2316.
(66) Slater, J. C. *The Calculation of Molecular Orbitals*; John Wiley & Sons: New York, 1979; p 104.

Table 6. Charge Decomposition of the Spin Unrestricted Linear Calculations on **1′(NO)**

																% for Fe		
level	occup	spin	orbital	energy (eV)	Fe	N1 (NO)	N2	N3	O1 (OH)	O2 (NO)	H1	H2	H3	H4	H5	H6	s	p	d
38A′	0.0	↓	d_{z^2}	−1.343	69	2	10	10	4	1	3	0	0	0	0	0	4	3	93
26A″	0.0	↓	d_{xy}	−1.808	76	0	14	0	5	0	3	0	0	0	0	0	0	0	100
25A″	0.0	↓	d_{yz}	−2.469	67	22	0	0	3	7	0	0	0	0	0	0	0	1	99
37A′	0.0	↓	d_{xz}	−2.478	67	22	1	0	2	7	0	0	0	0	0	0	0	1	99
13A″	0.0	↑	NO 2π	−2.735	10	59	3	0	2	25	0	0	0	0	0	0	0	15	85
18A′	0.0	↑	NO 2π	−2.742	11	59	2	0	2	25	0	0	0	0	0	0	0	15	85
36A′	0.0	↓	$d_{x^2-y^2}$	−3.164	85	0	0	0	14	0	0	0	0	0	0	0	0	0	100
24A″	1.0	↓	NO 2π	−4.568	10	24	1	0	52	13	0	0	0	0	0	0	0	1	99
35A′	1.0	↓	NO 2π	−4.622	11	24	2	4	45	13	0	0	0	0	0	0	0	1	98
3A″	1.0	↑	NO 1π	−12.560	5	28	5	0	1	54	0	0	0	3	2	0	0	17	83
7A′	1.0	↑	NO 1π	−12.563	5	28	6	0	1	53	1	0	0	3	1	1	2	17	81
16A″	1.0	↓	NO 1π	−13.544	3	35	1	0	0	60	0	0	0	0	0	0	0	26	74
26A′	1.0	↓	NO 1π	−13.544	3	35	1	0	0	60	0	0	0	0	0	0	0	26	73
6A′	1.0	↑	NO 5σ	−16.741	23	32	0	0	0	44	0	0	0	0	0	0	21	31	48
25A′	1.0	↓	NO 5σ	−17.646	21	34	0	0	0	44	0	0	0	0	0	0	22	35	43
5A′	1.0	↑	NO 4σ	−19.254	25	42	0	0	0	32	0	0	0	0	0	0	21	35	44
24A′	1.0	↓	NO 4σ	−20.235	22	43	0	0	1	33	0	0	0	0	0	0	19	38	42
1A′	1.0	↑	NO 3σ	−35.829	0	43	0	0	0	57	0	0	0	0	0	0	0	0	0
20A′	1.0	↓	NO 3σ	−37.351	0	43	0	0	0	57	0	0	0	0	0	0	0	0	0

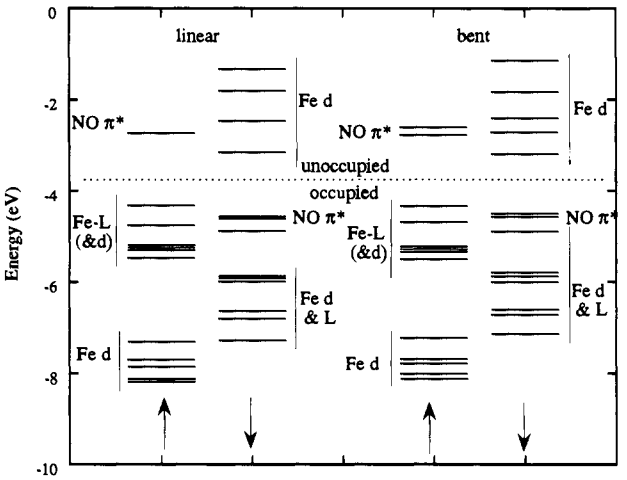

Figure 9. Energy level diagrams for spin unrestricted calculations on **1′(NO)** with both a linear (left) and bent (right) FeNO unit. In each calculation, the orbitals are divided into their spin up and spin down counterparts.

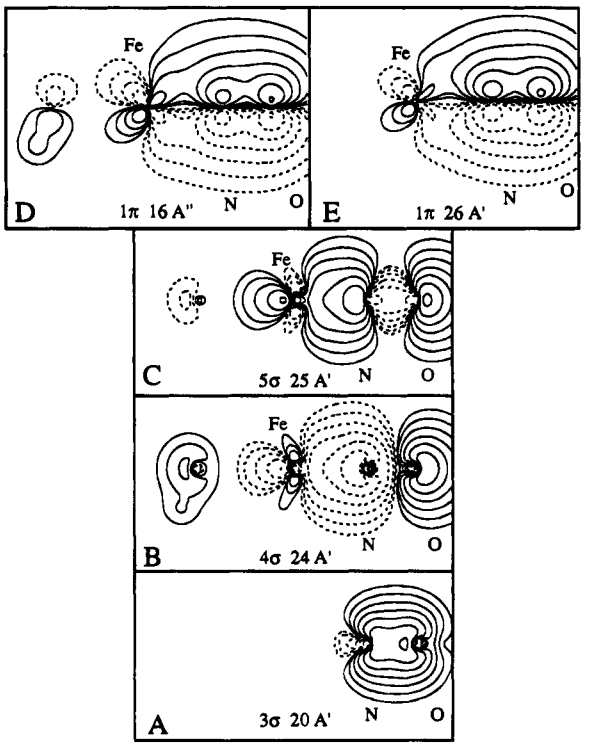

Figure 10. Contour plots of the predominantly NO bonding orbitals of the linear **1′(NO)** calculation.

can be found in the supplementary material as Figure S1. (Note that only the spin down orbitals are included in the diagram since the spin up orbitals are qualitatively similar but shifted in energy.) The NO σ bonding orbitals are $3\sigma^+$ and $5\sigma^+$ while the $4\sigma^+$ is NO σ^* antibonding. The 1π orbitals are NO π bonding and the 2π orbitals are NO antiboding. For a neutral NO molecule the orbital configuration is $(3\sigma^+)^2(4\sigma^+)^2(5\sigma^+)^2(1\pi)^4(2\pi)^1$. Since one electron resides in the antibonding 2π orbitals, the qualitative bond order is 2.5. These NO $C_{\infty v}$ orbital labels will be used in the following analysis which probes the bonding present in the $\{FeNO\}^7$ calculations. For a more rigorous description of NO bonding see ref 67.

In parallel to the spin restricted calculations, both linear and bent **1′(NO)** calculations have been performed. The linear calculation will be considered first. The energies and charge breakdown for the unoccupied Fe d orbitals and all of the NO orbitals for the linear calculation are given in Table 6. The spin down occupied Fe d orbitals and NO π^* orbitals are included in Figure 9 (linear). Note that in Figure 9 the orbitals are separated, with the spin up (↑) orbitals on the left and the spin down orbitals (↓) on the right. Also included in Figure 9 are the spin up occupied Fe d orbitals and the mixed Fe–L orbitals (L = NH_3, OH). The spin up Fe d orbitals are greatly stabilized in energy below their spin down counterparts (~6 eV). This stabilization has been observed previously in spin unrestricted calculations on *high spin ferric* complexes.[62–65] The NO π^* orbitals also split with the π^* spin down orbitals occupied and stabilized due to spin pairing with the Fe d_{xz} and d_{yz} orbitals, leading to an NO^- ($S = 1$). This spin pairing is due to direct orbital overlap, and thus the observed $S = 3/2$ ground state derives from antiferromagnetically coupling a high spin Fe^{3+} ($S = 5/2$) to an NO^- ($S = 1$).

In order to obtain a better picture of the bonding interactions in this complex, contour plots of the NO orbitals are shown in Figures 10 and 11. The occupied spin down orbitals of the NO ($3\sigma^+$, $4\sigma^+$, $5\sigma^+$, and 1π) are shown in Figure 10. Note that since the corresponding spin up orbitals are qualitatively

(67) Mulliken, R. S.; Ermler, W. C. *Diatomic Molecules: Results of ab initio Calculations*; Academic Press: San Francisco, 1977.

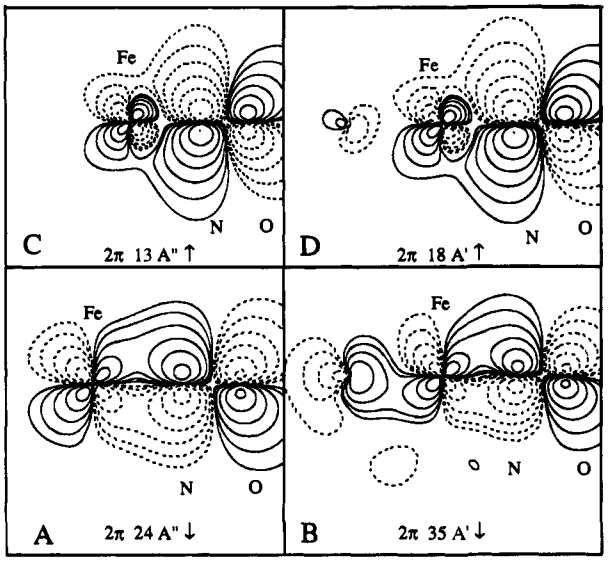

Figure 11. Contour plots of the predominantly NO π^* orbitals of the linear **1'(NO)** calculation.

very similar, they will not be discussed but are included in Table 6. The NO $3\sigma^+$ orbital shown in Figure 10A (level 20A' in Table 6) is localized solely on the NO and arises from NO 2s σ bonding orbitals. The NO $4\sigma^+$ (24A') and $5\sigma^+$ (25A') orbitals are the NO σ orbitals which are involved in bonding to the Fe. They are shown in Figure 10B,C, respectively. As listed in Table 6, levels 24A' and 25A' each contain >20% Fe character. This Fe character is distributed among the 4s, 4p, and 3d orbitals (see last columns in Table 6). The $4\sigma^+$ orbital is antibonding between the NO 2s orbitals, and the $5\sigma^+$ orbital is the bonding p_z interaction for the NO. The π bonding levels (1π) are given in Figure 10D,E. These orbitals are also π bonding with respect to the metal, but contain very little Fe character, ~3% (levels 16A" and 26A' in Table 6).

It is also important to consider the NO 2π antibonding orbitals. The contours of both the spin up and spin down 2π orbitals are shown in Figure 11. The occupied spin down orbitals, levels 24A" and 35A' in Table 6, are shown in Figure 11A,B. They are π bonding with respect to the Fe, but π antibonding with respect to the NO and have ~10% Fe d character. The unoccupied 2π orbitals, levels 13A" and 18A' in Table 6, are completely antibonding over the Fe–N–O moiety (Figure 11C,D). For completeness the unoccupied d orbitals which have NO character, the Fe d_{z^2}, Fe d_{xz}, and Fe d_{yz} orbitals, are given as supplementary material (Figure S2).

Since the complexes **1** and **2** have an FeNO angle of 156°, spin unrestricted calculations have also been performed on a bent FeNO structure which will be analyzed in a manner parallel to the linear calculation described above. The energy levels which result are given in Figure 9 (bent), and their energies and charge decomposition are given in Table 7. Again there are five unoccupied spin down orbitals that are predominantly Fe d in character while there are two unoccupied spin up NO π^* orbitals. The basic description of the electronic structure of the bent **1'(NO)** calculation is also d^5 Fe^{3+} $S = 5/2$ antiferromagnetically coupled to a NO^- $S = 1$.

Contour plots of the NO orbitals are given in Figures 12 and 13. The occupied spin down orbitals of the NO ($3\sigma^+$, $4\sigma^+$, $5\sigma^+$, and 1π) are shown in Figure 12. Since the spin up orbitals are very similar to the spin down orbitals, they will not be discussed but are included in Table 7. The NO $3\sigma^+$ orbital shown in Figure 12A (level 20A' in Table 7) is localized solely on the NO and arises from 2s σ bonding. The NO $4\sigma^+$ and

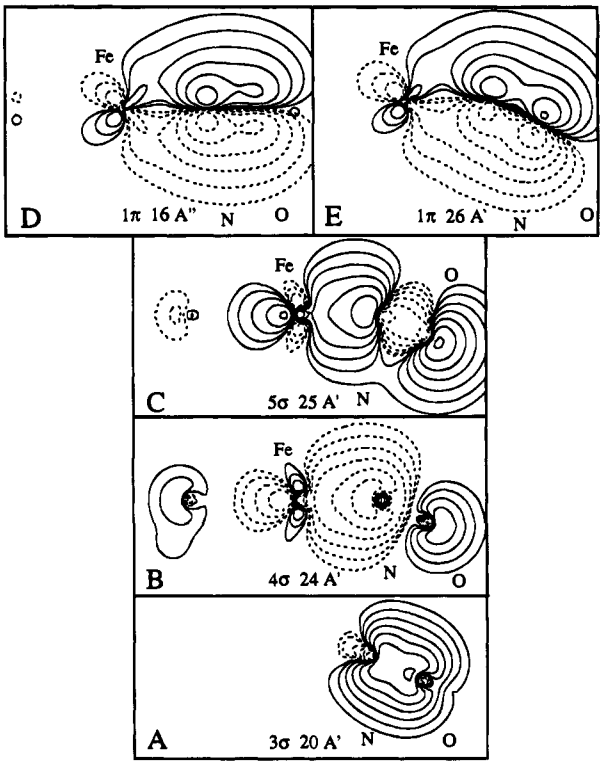

Figure 12. Contour plots of the predominantly NO bonding orbitals of the bent **1'(NO)** calculation.

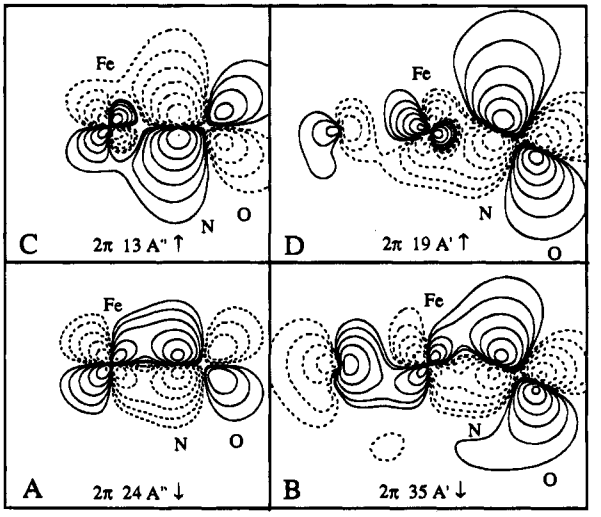

Figure 13. Contour plots of the predominantly NO π^* orbitals of the bent **1'(NO)** calculation.

$5\sigma^+$ orbitals are still the σ orbitals which are involved in bonding to the Fe. They are shown in Figure 12B,C, respectively. As listed in Table 7, levels 24A' and 25A' each contain a significant amount (>20%) of Fe character. This character is distributed over the 4s, 4p, and 3d orbitals of the Fe. The $4\sigma^+$ orbital is antibonding between the NO 2s orbitals and the $5\sigma^+$ orbital involves the bonding combination of p_z orbitals for the NO. These σ donor bonding orbitals appear to have changed very little upon bending the FeNO unit. The π bonding orbitals, *i.e.*, 1π, are given in Figure 12D,E. These orbitals also π bond to the metal, but they still contain very little Fe character, ~3% (levels 16A" and 26A' in Table 7). The 1π orbitals have also not changed significantly upon bending.

The NO 2π antibonding orbitals of the bent **1'(NO)** calculation are shown in Figure 13 for the spin up and spin down cases. The occupied spin down orbitals, levels 24A" and 35A' in Table

Table 7. Charge Decomposition of the Spin Unrestricted Bent Calculation on **1′(NO)**

																% for Fe		
level	occup	spin	orbital	energy (eV)	Fe	N1 (NO)	N2	N3	O1 (OH)	O2 (NO)	H1	H2	H3	H3	H5	H6	s	p	d
38A′	0.0	↓	d_{z^2}	−1.156	70	6	6	7	6	2	3	0	0	0	0	0	6	6	89
26A″	0.0	↓	d_{xy}	−1.832	76	0	15	0	5	0	3	0	0	0	0	0	0	0	100
25A″	0.0	↓	d_{yz}	−2.403	62	25	0	0	3	9	0	0	0	0	0	0	0	1	99
13A″	0.0	↑	NO 2π	−2.614	10	58	3	0	2	26	0	0	0	0	0	0	0	15	85
37A′	0.0	↓	d_{xz}	−2.723	72	16	1	0	3	6	0	0	0	0	0	0		1	98
19A′	0.0	↑	NO 2π	−2.786	22	49	0	1	3	23	1	0	0	0	0	0	12	20	68
36A′	0.0	↓	$d_{x^2-y^2}$	−3.199	84	0	0	0	15	0	0	0	0	0	0	0	0	0	100
24A″	1.0	↓	NO 2π	−4.503	15	24	1	0	45	13	0	0	0	0	0	0	0	1	99
35A′	1.0	↓	NO 2π	−4.588	12	24	3	9	37	14	0	0	1	0	0	0	4	17	79
3A″	1.0	↑	NO 1π	−12.357	6	28	6	0	1	52	1	0	0	3	2	0	0	17	83
7A′	1.0	↑	NO 1π	−12.386	6	29	7	0	2	50	1	0	0	3	1	1	5	17	78
16A″	1.0	↓	NO 1π	−13.236	3	35	1	0	1	50	0	0	0	0	0	0	0	27	73
26A′	1.0	↓	NO 1π	−13.272	3	36	1	0	1	58	0	0	0	0	0	0	4	27	69
6A′	1.0	↑	NO $5\sigma^+$	−16.351	23	33	0	0	0	44	0	0	0	0	0	0	21	30	48
25A′	1.0	↓	NO $5\sigma^+$	−17.156	22	36	0	0	0	42	0	0	0	0	0	0	23	35	42
5A′	1.0	↑	NO 4σ	−18.993	24	41	0	0	0	34	0	0	0	0	0	0	21	35	44
24A′	1.0	↓	NO 4σ	−19.863	21	41	0	0	0	36	0	0	0	0	0	0	20	38	42
1A′	1.0	↑	NO 3σ	−35.442	0	43	0	0	0	57	0	0	0	0	0	0	0	0	0
20A′	1.0	↓	NO 3σ	−36.814	0	43	0	0	0	57	0	0	0	0	0	0	0	0	0

Table 8. Transition State Calculations for Bent **1′(NO)**

donor	acceptor	energy (cm^{-1})
NO π^* (out-of-plane)	Fe d_{yz}	18 700
NO π^* (in-plane)	Fe d_{xz}	17 300
NO π^* (in-plane)	Fe $d_{x^2-y^2}$	13 450
Fe d_{xy}	Fe $d_{x^2-y^2}$	9 230

8, are shown in Figure 13A,B. They are π bonding with respect to the Fe, but π antibonding with respect to the NO. Note that, upon bending, there is a qualitative difference between the in-plane π interaction shown in Figure 13B and that shown in Figure 11B for the linear calculation. The contour in Figure 13B is no longer completely π in character and has acquired some σ contribution. While the percent Fe characters of these two orbitals are similar in both the linear and bent calculations (Tables 6 and 7), level 35A′ in the bent structure has acquired significant unoccupied Fe 4s and Fe 4p character compared to its linear counterpart, which is predominantly Fe 3d in character. Therefore, in the spin unrestricted calculation as in the spin restricted calculation this NO π^* orbital helps stabilize the bent FeNO unit through acquiring some σ bonding with an increase in Fe 4s and 4p character of this orbital which makes this a stronger bond. The unoccupied spin up $2\pi^*$ orbitals, levels 13A″ and 19A′, are completely antibonding over the Fe–N–O moiety (Figure 13C,D). Level 19A′ in the bent structure (Table 7), which should be compared to level 18A′ in the linear structure (Table 6) has doubled in Fe character and has also picked up more Fe 4s and 4p contributions (Table 7, right). For completeness the unoccupied Fe d_{z^2}, Fe d_{xz}, and Fe d_{yz} orbitals are included as supplementary material (Figure 3S).

Starting from the Fe^{3+} and NO^- limit, the FeNO bonding can now be examined. For Fe^{3+} all of the Fe d orbitals are half-occupied and available for participation in bonding. For an $S = 1$ NO^-, the $3\sigma^+$, $4\sigma^+$, $5\sigma^+$, and 1π orbitals are fully occupied and the 2π orbitals contain two unpaired electrons. The following discussion focuses on the calculation of the bent **1′(NO)** structure in Figures 12 and 13 and Table 7. In the crystal structure of **1**, the Fe–NO bond distance is 1.738 Å, which is much shorter than the other Fe^{3+}–ligand distances (average of 2.17 Å)[16] and indicative of a very strong bonding interaction between Fe^{3+} and NO^-. On the basis of the amount of Fe character in the predominantly NO orbitals in Table 7, the strongest Fe^{3+}–NO^- bonding interactions occur for the $4\sigma^+$ and $5\sigma^+$ orbitals, which are σ bonding to the metal (levels 24A′ and 25A′). Since the Fe character in these orbitals involves the Fe d_{z^2} orbital, this bonding interaction is partially compensated (or canceled) by the half-occupation of the antibonding Fe d_{z^2} orbital. The Fe character in both the $4\sigma^+$ and $5\sigma^+$ orbitals also has a sizable contribution from Fe 4s and Fe 4p which is not compensated since the antibonding Fe 4s and Fe 4p orbitals are not required. The major σ contributions to bonding result from interactions between the NO^- and Fe 4s and 4p orbitals. The Fe–NO π bonding described in the calculation derives mainly from the 2π orbitals rather than the 1π orbitals, since the spin down 2π orbitals have more Fe character (Table 7). This is smaller than the σ contribution and is further reduced by the half-occupation of the antibonding Fe d_{xz} and Fe d_{yz} orbitals which dominantly contribute to the metal character of the 2π spin down level. Therefore, the strength of the FeNO bond is due mainly to the NO^- $4\sigma^+$ and $5\sigma^+$ σ donor bonding interactions with the metal, with an additional π donor interaction involving the $2\pi^*$ level.

The experimental results presented above, in particular the edges and vibrational data, provide direct experimental evidence that the NO^- charge donation to the Fe^{3+} is large; *i.e.*, this cannot be considered an ionic structure. In particular, the X-ray absorption edge energy should be dependent upon the charge on the metal ion.[47] For complex **2**, the Fe K-edge is at 2 eV lower energy than that of the $[Fe(OH_2)EDTA]^-$ ferric analog. To obtain an experimental estimate of the charge on the NO, the *f*(NO) force constants for complexes **1** and **2** have been compared to those calculated from existing vibrational data on NO^+, NO, and NO^-, as described above. The *f*(NO) force constants for the complexes fall between those of NO^0 and NO^-, but are actually closer to that of NO^0. However, the pre-edge feature and the general shape of the edge features shown in Figure 1 indicate these complexes are more like Fe^{3+}. This is also supported by the assignment of the MCD and absorption spectra (*vide infra*) and is consistent with the results of the SCF-Xα-SW calculations. The important point here is the nature of the charge donation from the NO^- to the Fe^{3+}. Starting from the high spin Fe^{2+} and NO^0, and going to NO^-, an electron is donated from the Fe^{2+} to the $2\pi^*$ orbital of the NO which would weaken the NO molecular bond, as this orbital is π antibonding. However, starting from the Fe^{3+}–NO^- limit, charge donation from NO^- to the Fe^{3+} ion dominantly involves the $4\sigma^+$ and $5\sigma^+$ orbitals described above. The $4\sigma^+$ is NO antibonding, and donation from this orbital would lead to a stronger NO bond,

Scheme 1

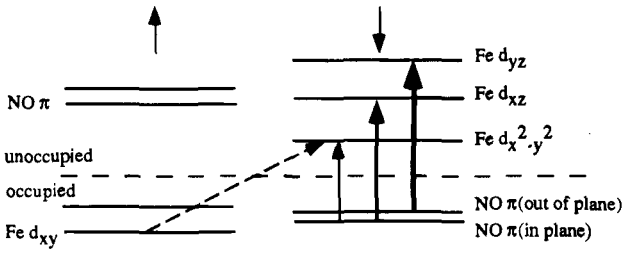

i.e., a larger force constant. Since this involves a σ antibonding orbital, its contribution to charge donation will be significantly more effective in strengthening the N−O bond than removal of electron density from the $2\pi^*$ orbital. The $5\sigma^+$ orbital, on the other hand, is bonding, and charge donation from this molecular orbital would destabilize the NO species, *i.e.*, reduce the force constant. Since from experiment the $\{FeNO\}^7$ force constants indicate that these complexes have a stronger NO bond than molecular NO^-, the $4\sigma^+$ orbital must dominate the Fe^{3+}−NO^- charge donation. Removal of charge from this antibonding orbital (and from the $2\pi^*$) stabilizes the N−O molecular bond, accounting for the observed high NO^- force constants.

(c) **Spectral Assignments.** In order to gain insight into the absorption and MCD spectral features of the $\{FeNO\}^7$ unit, transition state calculations have been performed in the SCF-Xα-SW formalism to obtain an energetic ordering of the electronic transitions. These transition state calculations give a resonable estimate of excitation energies, since they take into account the effects of relaxation.[61] In the transition state formalism, half an electron is removed from the donor orbital and placed in the acceptor orbital and the calculation is reconverged.[61] Since the experimental complexes being analyzed have a bent FeNO unit, the bent structure of **1′(NO)** is considered. As the ligand to metal charge transfer transition intensity depends on ligand−metal overlap,[68,69] Table 7 predicts that at low energy the most intense charge transfer (CT) transitions should involve the occupied spin down NO $2\pi^*$ orbitals, levels 24A″ and 35A′, as donor orbitals and the Fe d_{xz} and Fe d_{yz} orbitals, levels 25A″ and 37A′, as acceptor orbitals. The transition state calculations predict energies of 17 300 cm^{-1} for the in-plane NO $2\pi^* \rightarrow$ Fe d_{xz} transition and 18 700 cm^{-1} for the out-of-plane NO $2\pi^* \rightarrow$ Fe d_{yz} transition (Table 8). These transitions are illustrated in the spin unrestricted bonding scheme shown in Scheme 1 and based on Figure 9 where the arrow thickness reflects relative intensity based on overlap. There is no overlap of the in-plane NO $2\pi^*$ unit of the d_{yz} or of the out-of-plane NO $2\pi^*$ with the Fe d_{xz} orbital. A lower energy in-plane NO $2\pi^* \rightarrow$ Fe $d_{x^2-y^2}$ transition is calculated to be at 13 450 cm^{-1} (Table 8 and Scheme 1). Though also not predicted to have intensity based on the lack of overlap of the $d_{x^2-y^2}$ and no π^*, in the C_s symmetry of the bent structure the Fe $d_{x^2-y^2}$ orbital is allowed to mix with the d_{xz} orbital so the transition intensity can originate from the NO^- in-plane π^* orbital. These calculations predict the following charge transfer energy ordering for transitions with nonzero intensity: NO^- in-plane $2\pi^* \rightarrow$ Fe $d_{x^2-y^2}$ < NO^- in-plane $2\pi^* \rightarrow$ Fe d_{xz} < NO^- out-of-plane $\pi^* \rightarrow$ Fe d_{yz}. For comparison, transition state calculations on the linear **1′(NO)** NO $\pi^* \rightarrow$ Fe $d_{xz,yz}$ CT transitions are predicted to be nearly degenerate at ~20 000 cm^{-1}. As an estimate of the lowest energy high spin ferric spin forbidden ligand field (LF) transition, $^6A_1 \rightarrow {}^4T_1$ transition, a spin forbidden Fe d_{xy} (↑) → Fe $d_{x^2-y^2}$ (↓) excitation was also computed (Scheme 1, dashed arrow). This one electron transition is the only component of the $^6A_1 \rightarrow {}^4T_1$ transition that can be described by a single determinant.[62] It has an energy of 9230 cm^{-1} (Table 8).

We now can compare these predictions to the data. For complex **2**, both ferrous and ferric reference compounds exist which can be used to determine the existence of low energy CT transitions due to the EDTA ligation. Neither Fe^{2+}EDTA nor Fe^{3+}EDTA have CT transitions in this low energy region; thus, these bands cannot be assigned to EDTA → Fe^{3+} CT transitions. For complex **1**, the Me_3TACN also does not have CT transitions in this region[62] and the N_3^- CT transition at 22 700 cm^{-1} has been identified through resonance Raman excitation profiles. Therefore, the five transitions listed in Table 3 for both complexes must be due to the $\{FeNO\}^7$ unit.

Bands 1 and 2, the lowest energy transitions, do not enhance any of the Fe−N−O vibrations (Figures 6 and 7), indicating that they are unlikely to be $NO^- \rightarrow Fe^{3+}$ charge transfer transitions. Bands 1 and 2 are therefore assigned to LF transitions associated with the mainly ferric high spin site. The intensities of these features are weak, and the fact that band 3, which is even less intense than band 2 in complex **2**, does lead to Raman enhancement supports this assignment. These transitions are in the experimental range of the lowest energy LF transitions observed in ferric complexes, *i.e.*, the $^6A_1 \rightarrow {}^4T_1$ and $^4T_2$ transitions,[70] and the lowest energy LF transition (band 1) is within the energy range of the LF transition state energy calculated above (Table 8), 9230 *vs* 11 700 cm^{-1} for complex **1** (Table 3). An interesting feature of these LF transitions is that their intensities (15−300 mM^{-1} cm^{-1}) are an order of magnitude greater than that observed in normal ferric monomer complexes.[62,71,72] This can be attributed to two effects. These transitions in an isolated Fe^{3+} complex are $^6A_1 \rightarrow {}^4\Gamma$, which are spin forbidden. In the $\{FeNO\}^7$ complex, the $S = 5/2$ ground state couples to the NO^- $S = 1$ to form a $^4A_2$ ground state (in approximate C_{4v} symmetry, where z is the shorter Fe−NO bond). In the $\{FeNO\}^7$ $^4\Gamma$ excited states, the $^4\Gamma$ couples to the $S = 1$ NO^- to form $S_T = 5/2$, 3/2, and 1/2 excited states. Transitions from the $S = 3/2$ ground state to the $S = 3/2$ component of the excited state are effectively spin allowed. Thus, the coupling of the NO^- ($S = 1$) removes some of the spin forbiddeness of the normal high spin ferric LF transitions as is observed in ferric−oxo dimers.[62] A second source of intensity can be attributed to spin−orbit coupling of the LF transitions to the low energy $2\pi^*$ $NO^- \rightarrow Fe^{3+}$ charge transfer transitions through covalency. A similar spin−orbit intensity gaining mechanism has recently been shown to be dominant in ferric−oxo dimer complexes. This mechanism also preferentially enhances the ferric $^6A_1 \rightarrow {}^4T_2$ transition over the $^6A_1 \rightarrow {}^4T_1$ transition.[62] This is consistent with the lowest energy feature ($^6A_1 \rightarrow {}^4T_1$, band 1) being less intense than the next LF transition ($^6A_1 \rightarrow {}^4T_2$, band 2) in these Fe^{3+}−NO^- complexes.

As described above, resonance Raman profiles for both complexes (Figures 6C and 7C) indicate that the three higher energy transitions (bands 3−5) are in resonance with either metal−ligand Fe−NO or intraligand NO vibrations, demonstrating that distortions along these Fe−N−O vibrational modes occur upon excitation. Bands 3 and 4 for complex **2**, where the Raman profile is the cleanest, preferentially enhance the Fe−N−O bend. From their enhancement, all three of these bands are assigned as $NO^- \rightarrow Fe^{3+}$ charge transfer transitions. An energetic ordering of the three lowest energy CT transitions

(68) Solomon, E. I. *Comments Inorg. Chem.* **1984**, *3*, 255.
(69) Avoird, A. V. D.; Ros, P. *Theor. Chim. Acta* **1966**, *4*, 13.
(70) Lever, A. P. B. *Inorganic Electronic Spectroscopy*; Elsevier: New York, 1984; p 458.
(71) Holt, S.; Dingle, R. *Acta Chem. Scand.* **1968**, *22*, 1091.
(72) Lehmann, G. *Z. Phys. Chem. Neue Folge* **1970**, *72*, 279.

which should have nonzero intensity has been determined from the transition state SCF-Xα-SW calculations (Scheme 1, Table 8). Note that although the calculation on **1′(NO)** is based on complex **1** which is 6-coordinate, the same assignment can also be applied to **2** (which is expected to be 7-coordinate), with the experimental shift of the CT transitions to higher energy (Table 3) related to the shift in the d-manifold on going from 6- to 7-coordination. The lowest energy CT transition is predicted to be an NO^- in-plane $\pi^* \rightarrow Fe^{3+}$ $d_{x^2-y^2}$ (Scheme 1). As developed above, this transition should have little intensity since the Fe $d_{x^2-y^2}$ must mix with the d_π orbital in the bent structure to have overlap with the NO $2\pi^*$ (level 36A′ in Table 7). The next lowest energy transition is the (in-plane) NO^- $2\pi^* \rightarrow Fe^{3+}$ d_{xz} transition, with the out-of-plane NO^- $2\pi^* \rightarrow Fe^{3+}$ d_{yz} orbital next in energy (Scheme 1). Since absorption intensity depends on the amount of ligand character in the orbitals involved in these transitions,[68] the out-of-plane NO^- $\pi^* \rightarrow$ Fe d_{yz} transition is expected to be most intense (Table 7). This energy ordering and intensity pattern matches that of the CT transitions observed in Figures 6 and 7. Band 3, the lowest energy transition, is also lowest in intensity and can be assigned to the in-plane NO^- $2\pi^* \rightarrow Fe^{3+}$ $d_{x^2-y^2}$ CT transition. The two more intense CT transitions, bands 4 and 5, are assigned as the in-plane NO^- $2\pi^* \rightarrow$ Fe d_{xz} and the out-of-plane NO^- $2\pi^* \rightarrow$ Fe d_{yz} transitions. As predicted, the higher energy feature, band 5, is the most intense. The assignment is also consistent with the preferential resonance enhancement of bands 3 and 4 for the Fe–N–O bend compared to band 5 (Figure 6). The similar enhancement for bands 3 and 4 implies that these transitions involve the same change in electronic structure on excitation. They both originate from the in-plane NO^- $2\pi^*$ orbital, as opposed to band 5, which involves excitation from the out-of-plane NO^- $2\pi^*$ donor orbital. Comparison of the in-plane and out-of-plane π^* contours in Figure 13A,B indicates that the in-plane π^* orbital has picked up some σ character. As described above in Table 7, this σ character includes some Fe 4s and 4p contribution which is not present in the out-of-plane π^* orbital and only occurs upon bending. This stabilizes the in-plane π orbital and makes it a stronger bonding level in the bent structure. This is consistent with the fact that transitions involving this level enhance the Fe–N–O bend and provide direct experimental evidence for this in-plane π^* orbital stabilizing the bent structure.

(d) Spin Unrestricted Calculations on $\{FeO_2\}^8$. An energy level diagram of the spin down orbitals obtained from SCF-Xα-SW calculations on molecular O_2 (bond length 1.207 Å, Norman sphere radii) can be found in Figure S1 in the supplementary material. The O_2 σ bonding orbitals are $2\sigma_g^+$ and $3\sigma_g^+$ while the $2\sigma_u^+$ is O_2 σ antibonding. The $1\pi_u$ orbitals are O_2 π bonding, and the $1\pi_g$ orbitals are antibonding. For a neutral O_2 molecule, the orbital occupancy is $(2\sigma_g^+)^2(2\sigma_u^+)^2(3\sigma_g^+)^2(1\pi_u)^4$ $(1\pi_g)^2$. Thus, two electrons reside in the antibonding 1πg orbitals, giving a qualitative bond order of 2. The O_2 orbital $D_{\infty h}$ labels will be used in the following analysis probing the bonding present in the **1′(OO)** calculation. For a more detailed analysis of molecular O_2 see ref 67.

Since non-heme $\{FeO_2\}^8$ species have not been structurally characterized, the geometry of **1′(OO)** is based on the analogous heme–oxygen complexes with an O_2 bond length of 1.25 Å, an Fe–O bond length of 1.75 Å, and an FeO_2 angle of 135° (Figure 14, top).[40,41] Also in the FeO_2 calculation, there is a question of spin state, since no experimental evidence presently exists. There are four possibilities for eight electrons in the five Fe and two O_2 valence orbitals corresponding to $S = 0$, 1, 2, and 3. Most non-heme iron enzyme structures are high spin,

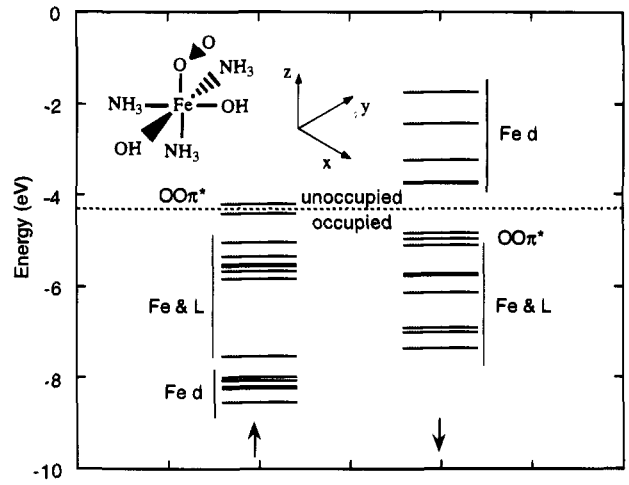

Figure 14. Energy level diagram for **1′(OO)**. The orbitals are divided into the spin up and spin down counterparts. Shown at the top are the core atoms and coordinate frame for **1′(OO)**. The molecular coordinate frame has z along the Fe–OO.

and the $S = 0$ spin state can be eliminated in considering these cases. (Note that there are instances where non-heme Fe biological systems, e.g., bleomycin[73a] and nitrile hydratase,[73b] have resting low spin ferric sites; these low spin cases will be considered in a future study.) An $S = 3$ spin state would necessarily involve ferromagnetic coupling of unpaired O_2 electrons with those on the Fe. This is not realistic on the basis of the electronic structure description given above which has shown that the unpaired electrons on the NO (or O_2) would have to be spin paired due to direct orbital overlap. Calculations were performed on the two likely spin states, $S = 1$ and $S = 2$. The $S = 2$ ground state is supported by the SCF-Xα-SW calculations since it corresponds to a description where the unoccupied orbitals are at highest energy, which is not the case for the $S = 1$ alternative. The energies and charge breakdown for the unoccupied Fe d orbitals and all of the O_2 orbitals for the $S = 2$ calculation are shown in Table 9. The spin down occupied Fe d orbitals and O_2 π^* orbitals are shown in Figure 14. Note that in Figure 14 the orbitals are separated, with the spin up on the left and the spin down on the right, as used previously for these spin unrestricted calculations. Also included are the spin up occupied Fe d orbitals and the Fe–L (where L = NH_3, OH^-) orbitals. The spin up Fe d orbitals are again greatly stabilized below their spin down counterparts (~6 eV) which is consistent with a *high spin ferric* description of the Fe.[62–65] (Note that a calculation with a longer Fe–O bond length (1.85 Å) gives an identical electronic structure description.)

Inspection of Figure 14 and Table 9 reveals that the five unoccupied spin down orbitals are predominantly Fe d in character while the unoccupied spin up orbital (19A′) is an O_2 $1\pi_g^*$ orbital. Thus, as for the NO calculations, there are five uncompensated Fe d orbitals. In this case, there is only one uncompensated O_2 π^* orbital. This leads to a description of the electronic structure of the $\{FeO_2\}^8$ unit as $S = 5/2$ d^5 Fe^{3+} antiferromagnetically coupled to an $S = 1/2$ O_2^- to obtain the $S = 2$ ground state.

In order to describe the bonding interactions in **1′(OO)**, contour plots of the O_2 orbitals have been made. These are shown in Figures 15 and 16. The spin down occupied orbitals of the O_2^-, $2\sigma_g^+$, $2\sigma_u^+$, $3\sigma_g^+$, and $1\pi_u$, are shown in Figure 15.

(73) (a) Sugiura, Y. *J. Am. Chem. Soc.* **1980**, *102*, 5208. (b) Sugiura, Y.; Kuwahara, J.; Nagasawa, T.; Yamada, H. *J. Am. Chem. Soc.* **1987**, *109*, 5848.

Table 9. Charge decomposition of the spin unrestricted bent calculation on **1′(OO)**

																% for Fe		
level	occup	spin	orbital	energy (eV)	Fe	O1 (O_2)	N2	N3	O2 (OH)	O3 (O_2)	H1	H2	H3	H4	H5	H6	s	p	d
38A′	0.0	↓	d_{z^2}	−1.731	74	7	5	6	3	3	2	0	0	0	0	0	2	3	95
26A″	0.0	↓	d_{xy}	−2.434	74	0	17	0	5	0	3	0	0	0	0	0	0	0	100
25A′	0.0	↓	d_{yz}	−3.222	62	19	0	0	6	12	0	0	0	0	0	0	0	1	99
37A′	0.0	↓	d_{xz}	−3.730	79	4	1	0	12	4	0	0	0	0	0	0	0	1	99
36A′	0.0	↓	$d_{x^2-y^2}$	−3.754	78	0	0	0	22	0	0	0	0	0	0	0	0	0	100
19A′	0.0	↑	OO $1\pi_g$	−4.198	38	19	8	11	3	19	1	0	0	0	0	0	4	5	90
13A″	1.0	↑	OO $1\pi_g$	−4.420	8	38	8	0	0	45	0	0	0	0	0	0	0	1	99
24A″	1.0	↓	OO $1\pi_g$	−4.835	8	19	0	0	51	21	0	0	0	0	0	0	0	1	99
35A′	1.0	↓	OO $1\pi_g$	−5.111	6	20	2	11	30	30	0	0	1	0	0	0	13	55	31
7A″	1.0	↑	OO $1\pi_u$	−10.846	21	28	4	1	19	18	6	0	1	2	0	0	0	0	100
19A″	1.0	↓	OO $1\pi_u$	−10.872	8	39	4	0	12	28	5	0	0	2	1	0	0	41	59
29A′	1.0	↓	OO $1\pi_u$	−11.275	9	39	7	0	12	23	5	0	0	3	0	2	40	35	25
10A′	1.0	↑	OO $1\pi_u$	−11.543	9	22	15	8	14	11	5	4	2	6	0	5	37	23	41
25A′	1.0	↓	OO $3\sigma_g$	−13.970	13	34	0	0	0	52	0	0	0	0	0	0	25	30	45
6A′	1.0	↑	OO $3\sigma_g$	−14.207	15	32	0	0	0	52	0	0	0	0	0	0	20	24	57
24A′	1.0	↓	OO $2\sigma_u^+$	−20.562	19	46	1	0	0	33	0	0	0	0	0	0	20	38	43
5A′	1.0	↑	OO $2\sigma_u^+$	−20.825	21	45	1	1	0	32	0	0	0	0	0	0	19	36	45
20A′	1.0	↓	OO $2\sigma_g^+$	−30.579	3	52	0	0	0	45	0	0	0	0	0	0	21	40	39
1A′	1.0	↑	OO $2\sigma_g^+$	−30.701	4	53	0	0	0	44	0	0	0	0	0	0	21	39	40

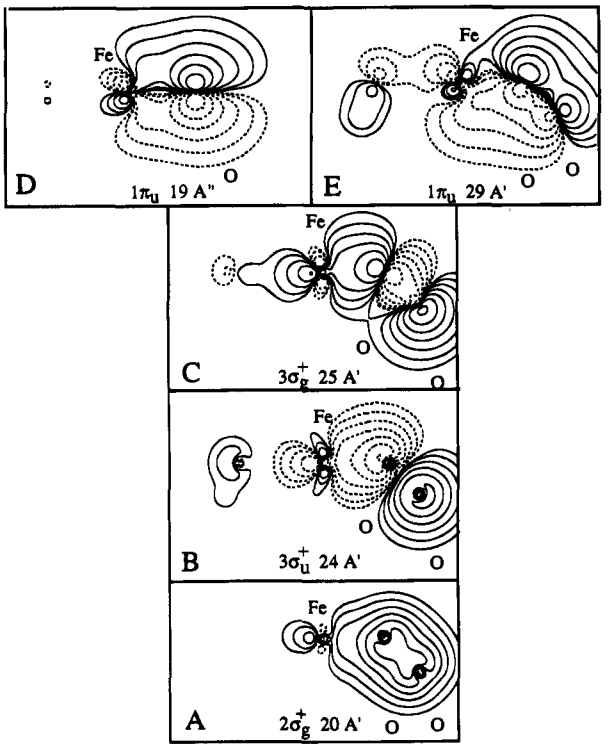

Figure 15. Contour plots of the predominantly OO bonding orbitals of the bent **1′(OO)** calculation.

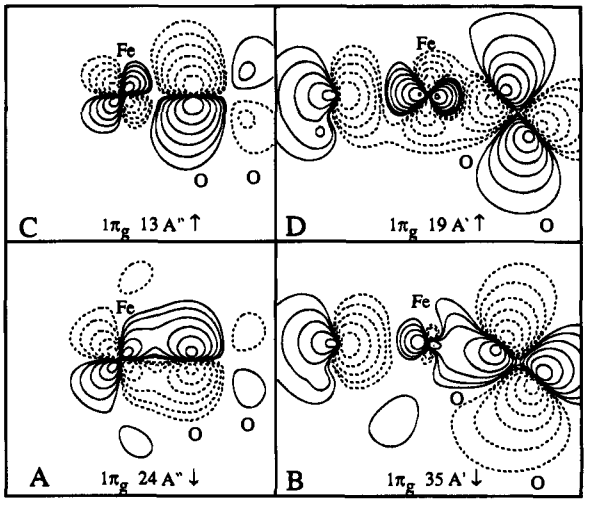

Figure 16. Contour plots of the predominantly OO π^* orbitals of the bent **1′(OO)** calculation.

Again, note that the spin up orbitals are qualitatively very similar and will not be discussed but are included in Table 9. The O_2^- $2\sigma_g$ orbital shown in Figure 15A, level 20A′ in Table 9, is localized on the O_2^-, with a very small amount of Fe character, and arises from O_2 2s σ bonding. The O_2^- $2\sigma_u^+$ and $3\sigma_g^+$ orbitals are the O_2 σ orbitals which are involved in bonding to the Fe^{3+}. They are shown in Figure 15B,C, respectively. As listed in Table 9, the $2\sigma_u^+$ orbital (level 24A′), which is antibonding with respect to the O−O bond, contains ~20% Fe character as does the similar orbital in FeNO; see level 24A′ in Table 7. On the other hand, the $3\sigma_g^+$ bonding orbital, level 25A′ in Table 9, no longer contains as much Fe character as the equivalent FeNO orbital, level 25A′ in Table 7 (13% vs 21%). The Fe character in both of these levels is divided among the Fe 4s, 4p, and 3d orbitals; see the last columns in Table 9. The $2\sigma_u^+$ orbital is antibonding between the O_2 2s orbitals and the $3\sigma_g^+$ orbital is the bonding combination of p_z orbitals for O_2^-. The π bonding $1\pi_u$ orbitals are given in Figure 15D,E. These orbitals are also bonding with respect to the metal and contain more Fe character than their NO counterparts, ~9% (O_2) *vs* ~3% (NO) (levels 16A″ and 26A′ in Table 9 (O_2) *vs* levels 16A″ and 26A′ in Table 7 (NO)).

The contours of both the spin up and spin down O_2 $1\pi_g$ partially occupied π antibonding orbitals are shown in Figure 16. The occupied spin down orbitals, levels 24A″ and 35A′ in Table 9, are shown in Figure 16A,B. The out-of-plane FeO_2 orbital, level 24A″ is π bonding with respect to the Fe, but the in-plane orbital, level 35A′, is found to have a mainly σ bonding interaction with the Fe. Both orbitals are π antibonding with respect to the O−O bond. These orbitals contain less Fe character than their NO counterparts. The occupied spin up $1\pi_g$ orbital, level 13A″, shown in Figure 16C is slightly lower in energy than the corresponding in-plane unoccupied O_2 $1\pi_g$ orbital, level 19A′ in Table 9. Both of these latter orbitals are completely antibonding over the Fe−O−O moiety (Figure 16C,D). The unoccupied Fe d_{z^2}, Fe d_{xz}, and Fe d_{yz} orbital contours are included as supplementary material (Figure S4).

The results of the calculations on the bent structure **1′(NO)** and that of **1′(OO)** can be compared to gain insight into the differences in the bonding of an O_2 bound species compared to

an NO bound species where the bonding description from these calculations has been supported by experiment. Overall the intramolecular O_2^- bond should be weaker than the intramolecular NO^- bond due to the extra electron in the π^* orbitals. Looking at the specific orbital bonding interactions of the O_2^- with the Fe^{3+}, the main σ donor bonding interactions are from the $2\sigma_u^+$ and $3\sigma_g^+$ orbitals, levels 24A′ and 25A′ in Table 9, which can be compared to the $4\sigma^+$ and $5\sigma^+$ orbitals, respectively, of NO (levels 24A′ and 25A′ in Table 7). The $3\sigma_g^+$ has less Fe character which induces a somewhat weaker σ bond between the Fe and O_2. Thus, the $2\sigma_u^+$ orbital which is antibonding with respect to the O–O bond is the orbital most strongly involved in σ donor bonding to the Fe^{3+}. The corresponding $4\sigma^+$ orbital for NO^- is also the main Fe^{3+}–NO^- bonding orbital (*vide supra*). This means that a similar metal–ligand σ donor bonding interaction exists in both the $\{FeNO\}^7$ and $\{FeO_2\}^8$ species. As was observed for the Fe^{3+}–NO^- calculations, the Fe^{3+}–O_2^- π bonding interactions are not as strong as the σ interactions, and in fact the sum of the Fe–O_2 π bonding orbitals should be similar for the $\{FeO_2\}^8$ and $\{FeNO\}^7$ systems. However, there is an extra electron in the $\{FeO_2\}^8$ compared to the $\{FeNO\}^7$ species. This electron resides in the $1\pi_g$ orbital which is Fe^{3+}–O_2^- π antibonding and would lead to weaker Fe^{3+}–O_2^- π bonding. The most significant change in replacing the NO with O_2 is that the spin down π^* ($1\pi_g$) orbitals of the O_2 are more stable relative to the d orbitals than for NO. (This is also observed in the free NO and O_2 calculations shown in Figure S1 and in experiments.)[74] This allows the extra electron present in the **1′(OO)** calculation to occupy the out-of-plane O_2 π^* orbital, leading to the electronic structure description of $S = 5/2$ Fe^{3+} antiferromagnetically coupled to a superoxide O_2^- ($S = 1/2$). Finally, the calculations can also be used to obtain the relative charges on the two oxygens of the O_2^-.[41] These indicate that the O atom not bound to the Fe has ~0.4 more charge than the Fe bound O atom. This is attributed to the strong σ bonding interaction with the Fe. This polarization of the O_2^- bond should have a significant effect on its reactivity.

Since the SCF-Xα-SW calculations are able to predict an $NO^- \rightarrow Fe^{3+}$ CT spectrum in good agreement with experiment, they can also be used to predict expected $O_2^- \rightarrow Fe^{3+}$ charge transfer transitions in possible oxygen intermediates. The in-plane O_2^- $1\pi_g^* \rightarrow$ Fe d_{xz} transition (level 35A′ to level 37A′ in Table 9) is calculated to be at 13 000 cm^{-1}, with the out-of-plane O_2^- $1\pi_g^* \rightarrow$ Fe d_{yz} transition (level 24A′ to level 25A′ in Table 9) estimated to occur at 14 350 cm^{-1}. As for the **1′(NO)** calculation, the out-of-plane $\pi^* \rightarrow$ Fe d_π transition is predicted to be at higher energy and with more intensity on the basis of the amount of superoxide character in the acceptor d orbital.[68,69] These transitions are predicted to occur at lower energies, ~3000 cm^{-1} less than equivalent transitions in a Fe^{3+}–NO^- complex, and should overlap with the lower energy LF transitions which will also be present in this high spin ferric complex but with the ligand field bands lower in intensity.

Discussion

The theoretical and experimental electronic structure description we have developed for the $\{FeNO\}^7$ $S = 3/2$ non-heme iron complex involves a high spin Fe^{3+} $S = 5/2$ ion antiferromagnetically coupled to an NO^- ligand with $S = 1$. From the SCF-Xα-SW calculations, the high spin ferric description derives from the large exchange stabilization of the d^5 configuration. In the spin unrestricted calculations, which allow spin up and spin down electrons to occupy different orbitals, the occupied spin up d orbitals are stabilized below the unoccupied spin down counterparts by 6 eV due to this exchange interaction. The occupied spin down NO π^* orbitals are stabilized due to their direct overlap with the spin up iron d_{xz} and d_{yz} orbitals. Thus, this orbital overlap leads to an $S = 1$ on the NO^- unit and its antiferromagnetic coupling to the high spin ferric center. Experimental support for this description comes from XAS, resonance Raman, and absorption/MCD/resonance Raman profile excited state spectroscopies. From the XAS, the single pre-edge peak at ~7113 eV, rather than two peaks split by 1.9 eV as in the ferrous complexes, and the shape and energy of the rising edge both indicate that the iron is in the high spin ferric oxidation state. Further the first shell EXAFS distances of the NO complex are ~0.1 Å shorter than those of the ferrous complex with corresponding ligation but very close to those of the ferric analog.[21] From resonance Raman spectroscopy, the intraligand frequency of ~1750 cm^{-1} combined with metal–ligand vibrational data on the Fe–NO unit and a normal coordinate analysis give an NO stretching force constant which, compared to molecular NO species, is significantly reduced, indicating electron transfer into the NO π^* orbital resulting in an NO^- species. From excited state spectroscopies, the ligand field and CT transitions have been identified using resonance Raman profiles. The ligand field transition energies are consistent with those observed for high spin ferric complexes, and the CT transitions are in an energy range and ordering consistent with predictions from the SCF-Xα-SW electronic structure calculations for NO^- $\pi^* \rightarrow Fe^{3+}$ d CT transitions. Additional support of this description derives from ground state EPR and Mössbauer spectroscopic studies, by Arciero *et al.*[7] and Orville *et al.*,[75] respectively, where no N or O superhyperfine coupling is observed and the metal hyperfine coupling is found to be anisotropic. As the two unpaired electrons on the NO^- are spin paired with the Fe $d_{xz,yz}$ electrons, the $S = 3/2$ of the Fe^{3+}–NO^- unit involves the $(d_{xy})^1$, $d(_{x^2-y^2})^1$, and $(d_{z^2})^1$ electrons. These do not delocalize into the NO^- unit and thus do not couple to the N or O nuclei, and would produce an anisotropic spin distribution in the *xy* plane with a dipolar hyperfine coupling to the nuclear spin on the iron which has a negative principle component.

Our data further show that starting from the Fe^{3+}–NO^- limit the NO^- is involved in a strong donor bonding interaction to the Fe^{3+} which results in a highly covalent Fe^{3+}–NO^- bond. First, from magnetic susceptibility the electrons of the NO^- are strongly antiferromagnetically coupled to the iron to give the $S = 3/2$ spin state which requires significant orbital overlap. Second, the rising edges of the XAS spectra of the Fe^{3+}–NO^- complexes are at lower energy than the respective ferric complexes, even when ligand field effects on the 4p orbitals are taken into account, indicating charge donation from the NO^- to the ferric center. Finally, the intraligand frequency and calculated force constant are significantly higher than those found for molecular NO^-, again indicating charge donation from an antibonding orbital on the NO^- of the iron–nitrosyl complex. Our spin unrestricted SCF-Xα-SW calculations provide insight into the nature of the strong Fe^{3+}–NO^- bond. In particular from Table 7, there are two strong donor interactions which are, in fact, σ in character. These involve the NO^- $4\sigma^+$ and $5\sigma^+$ orbitals. The former is σ antibonding with respect to the NO^- and dominates the charge donation to the Fe^{3+} due to better overlap (*i.e.*, greater N character in the antibonding NO molecular orbital). This charge donation thus removes electron density from a strongly antibonding orbital, which significantly

(74) Turner, D. W.; Baker, C.; Baker, A. D.; Brundle, C. R. *Molecular Photoelectron Spectroscopy*; Wiley-Interscience: London, 1970; p 55.

(75) Orville, A. M.; Chen, V. J.; Kriauciunas, A.; Harpel, M. R.; Fox, B. G.; Münck, E.; Lipscomb, J. D. *Biochemistry* **1992**, *31*, 4602.

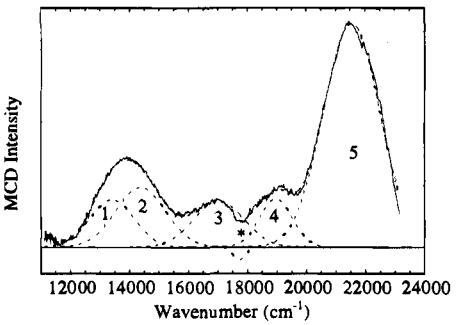

Figure 17. MCD spectrum and Gaussian resolution of SBL−NO at 4.2 K and 5 T in 0.1 M pH 7.6 HEPES buffer and 50% glycerol. The asterisk indicates a feature due to a <1% heme impurity.

increases the strength of the intramolecular NO^- bond, leading to the large increase in the bound NO force constant observed experimentally. It is important to emphasize that reduction of the NO by the ferrous complex involves electron transfer into the NO π^* orbital while charge donation of the bound NO^- to the Fe^{3+} dominantly involves electron transfer from an NO σ^* orbital. Thus, charge donation from the bound NO^- to the Fe^{3+} can significantly increase the strength of the NO bond.

Insight into the π bonding interactions is available from the CT region in Figures 6 and 7. We have assigned bands 3−5 as NO^- $\pi^* \rightarrow$ Fe d CT transitions. In ref 62, it has been shown that the intensity of the ligand to metal CT transitions can be used to quantitate the donor ability of that bond. The fact that these three transitions are fairly weak ($\epsilon < 1000\ M^{-1}\ cm^{-1}$) is consistent with a more limited π donor interaction into the Fe d orbitals as found in the electronic structure calculations. From Figure 6, bands 3 and 4 show strong resonance enhancement of the Fe−NO bend. Both transitions involve excitation from the 35A′ orbital in Figure 13 which is the in-plane NO^- π^* bonding interaction with the Fe d_{xz} orbital. Thus, this bonding interaction must be responsible for the bent Fe−NO bond which is observed experimentally with an angle of 156°. The spin restricted calculation in Figure 8 shows that this orbital is stabilized in energy in the bent structure, while in the spin unrestricted calculation this orbital picks up a σ component with unoccupied Fe 4s and 4p character on bending which leads to a stronger Fe−NO bond. The MCD spectra of the ligand field and the CT region are particularly useful in correlating model data to the nitrosyl derivatives of the non-heme iron protein active sites. In Figure 17 we compare the MCD spectrum of complex **1** to that of the nitrosyl derivative of soybean lipoxygenase which also has a $S = 3/2$ ground state.[5] The $\{FeNO\}^7$ lipoxygenase MCD spectrum directly parallels that of complex **1**, indicating that the protein active site should also be described as bent Fe^{3+}−NO^- with a parallel assignment of the specific spectral features (bands 1−5 in Figures 6, 7, and 17). Spectral data of NO derivatives of other non-heme iron enzymes are now required to establish this electronic structure description for these centers and to quantitate differences in Fe−NO bonding which could relate to differences in reactivity.

On the basis of the studies presented above, the spin unrestricted SCF-Xα-SW electronic structure calculations provide a description of the bonding which is in very good agreement with a wide range of experimental data on the stable $S = 3/2$ iron−nitrosyl complexes. We can then use these calculations to obtain insight into the Fe−O_2 bonding in possible oxygen intermediates and its relation to activation. The bonding description generated for a bent end-on $\{FeO_2\}^8$ complex involves reduction of O_2 to generate an iron−superoxide complex that is Fe^{3+} $S = 5/2$ antiferromagnetically coupled to an O_2^- $S = 1/2$. Again the high spin ferric electronic structure derives from the exchange splitting of the d orbitals in this spin unrestricted calculation, and the antiferromagnetism comes from overlap between the O_2^- in-plane π^* orbital which contains the unpaired electron and the Fe d_{xz} orbital. In parallel with the Fe^{3+}−NO^- bonding description, the O_2^- is involved in significant σ charge donation to the Fe^{3+} through the O_2^- $2\sigma_u^+$ which (as for the $4\sigma^+$ of NO^-) is σ antibonding with respect to the O_2^- bond. Thus, spectral data on the nitrosyl complex of the non-heme active sites in proteins can be used to obtain insight into the bonding of the initial superoxide intermediate which may be formed in the reaction of the ferrous site with dioxygen. In particular, normal coordinate analysis of the resonance Raman data provides an NO stretching force constant which directly reflects the strength of this dominant σ donor interaction of the NO^- (and O_2^-) with the Fe^{3+}. These electronic structure calculations also provide insight into the activation of the bound superoxide for further reaction or reduction. The strong σ donation shifts electron density off the superoxide and strengthens the O−O bond relative to free superoxide. The strong bonding to the Fe^{3+} polarizes the O−O bond such that there is increased negative charge on the unbound O atom. These studies are now being extended to nitrosyl derivatives of other non-heme iron enzymes to define small molecule bonding diffeences which could contribute to differences in dioxygen reactivity.

Acknowledgment. This research was supported by grants from the NIH (GM40392, to E.I.S.) and NSF (CHE-9121576, to K.O.H.). The Stanford Synchrotron Radiation Laboratory is supported by the Department of Energy, Office of Basic Energy Sciences, Divisions of Chemical Science and Materials Science, and in part by the National Institutes of Health, National Center for Research Resources, Biomedical Research Technology Program (Grant RR-01209, to K.O.H.), and the DOE's Office of Health and Environmental Research.

Supplementary Material Available: Figures showing the energy level diagram from SCF-Xα-SW calculations of molecular NO and O_2 and contour plots of the predominantly Fe d orbitals for linear and bent **1′(NO)** and bent **1′(OO)** and tables giving the molecular input parameters for the **1′(NO)** and **1′(OO)** calculations (6 pages). This material is contained in many libraries on microfiche, immediately follows this article in the microfilm version of the journal, and can be ordered from the ACS; see any current masthead page for ordering information.

JA942757U